Photoemission study of mixed-valence Mn oxides

Thesis

Kazuaki Ebata

Department of Complexity Science and Engineering,
Graduate School of Frontier Sciences,
University of Tokyo

December, 2007

Contents

1 Introduction 5

2 Experimental methods 19
- 2.1 Principle of photoemission spectroscopy . . . 19
  - 2.1.1 General formulation . . . 19
  - 2.1.2 Resonant photoemission spectroscopy . . . 22
  - 2.1.3 Electron escape depth . . . 23
- 2.2 Photoemission measurement system . . . 24
- 2.3 Surface preparation for ultraviolet photoemission spectroscopy 26
- 2.4 Chemical potential shift . . . 26

3 Doping dependence of chemical potential and spectral-weight transfer in $Pr_{1-x}Ca_xMnO_3$ 31
- 3.1 Introduction . . . 31
- 3.2 Experimental . . . 34
- 3.3 Results and discussion . . . 36
  - 3.3.1 Chemical potential shift . . . 36
  - 3.3.2 Spectral-weight transfer near Fermi level (E_F) . . . 44
- 3.4 Conclusion . . . 47

4 Temperature dependence of chemical potential and spectral-weight transfer in $Pr_{1-x}Ca_xMnO_3$ 53
- 4.1 Introduction . . . 53
- 4.2 Experimental . . . 56
- 4.3 Results and discussion . . . 57
  - 4.3.1 Valence-band spectra . . . 57
  - 4.3.2 Chemical potential shift . . . 60
  - 4.3.3 Spectral-weight transfer near Fermi level (E_F) . . . 63
- 4.4 Conclusion . . . 63

5 Doping dependence of chemical potential in $Nd_{1-x}Sr_xMnO_3$ 67
- 5.1 Introduction . . . 67

5.2 Experimental 68
5.3 Results and discussion 69
5.4 Conclusion 72

6 Temperature dependence of chemical potential in $Nd_{1-x}Sr_xMnO_3$ 75
6.1 Introduction 75
6.2 Experimental 79
6.3 Results and discussion 79
6.4 Conclusion 85

7 Effects of filling and bandwidth control on the chemical potential in manganites 93
7.1 Introduction 93
7.2 Experimental 93
7.3 Results and discussion 94
7.4 Conclusion 99

8 Observation of photoinduced effects in manganites studied by x-ray photoemission spectroscopy 103
8.1 Introduction 103
8.2 Experimental 105
8.3 Results and discussion 106
8.3.1 $Pr_{1-x}Ca_xMnO_3$ 106
8.3.2 $Nd_{1-x}Sr_xMnO_3$ 110
8.4 Conclusion 113

9 Summary and future prospects 117

Acknowledgments 125

Chapter 1

Introduction

Perovskite-type transition-metal oxides (TMO) have been attracting much interest because of their variety of magnetic, electrical and structural properties [1.1]. The high-temperature superconducting cuprates with layered perovskite structures were discovered about 20 years ago, which was the first renewal of interest in the perovskite-type TMO [1.2]. Extensive studies in the TMO have revealed that strong electron-electron correlation generally plays an important role. Band filling and bandwidth in these materials, which are experimentally varied by chemical composition, pressure, magnetic fields, and so on, are two important parameters.

The perovskite manganese oxides (manganites) with chemical compositions $R_{1-x}A_x\mathrm{MnO_3}$, where R is a rare-earth metal (R = La, Nd, Pr) and A is an alkaline-earth metal (A = Sr, Ba, Ca), are a typical example of TMO. Colossal magnetoresistance (CMR) as shown in Fig. 1.1 and spin, charge and orbital ordering [1.3, 4, 5, 6, 7, 8] have been observed in the manganites. The electronic configuration of the $\mathrm{Mn^{3+}}$ ion is high-spin $t_{2g}^3 e_g^1$ (total spin of $S = 2$) as shown in Fig. 1.2. The crystal field splitting between the t_{2g} and e_g levels is about 1 eV. Hund's-rule coupling energy is as large as 2-3 eV for manganites. The substitution of A^{2+} for R^{3+} at the A-site controls the mean valence of Mn. Upon hole doping, the e_g electrons can hop depending on the relative configurations of the local spins and therefore play a role of conduction carriers.

Historically, the magnetic and transport properties of the maganites have been discussed in terms of double-exchange (DE) mechanism with the localized t_{2g} electrons and the itinerant e_g electrons [1.9, 10]. In this mechanism, the kinetic energy gain of the doped holes is maximized when all of the e_g and t_{2g} electrons have parallel spins, which gives rise to ferromagnetic interaction (see, Fig. 1.3). The model Hamiltonian for such a system is given

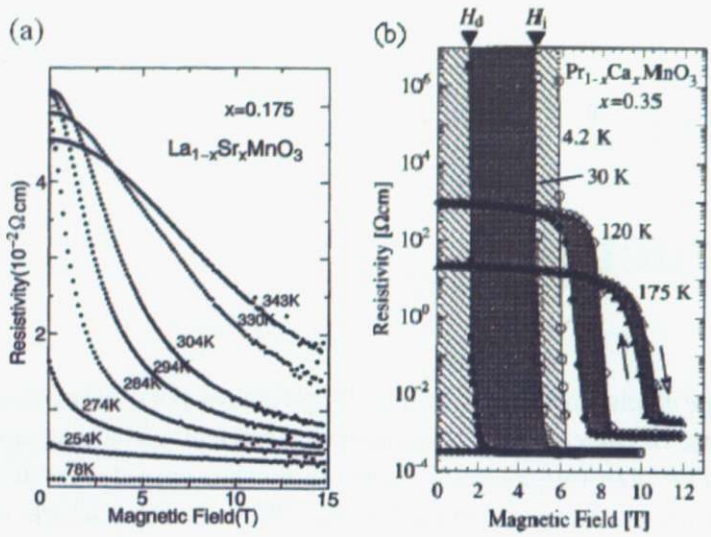

Figure 1.1: CMR effect in manganites: (a) $La_{1-x}Sr_xMnO_3$ ($x = 0.175$) taken at various temperatures [1.3, 4]. (b) $Pr_{1-x}Ca_xMnO_3$ ($x = 0.35$) taken at 175, 120, 30 and 4.2 K [1.5].

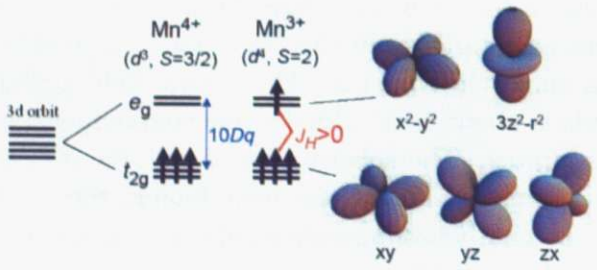

Figure 1.2: Electronic structure of the Mn ion in manganites [1.8]. The degenerate d levels are split into doubly degenerate e_g levels and triply degenerate t_{2g} levels due to the cubic crystal field. Because the crystal field splitting ($10\,Dq$) is smaller than the Hunt coupling (J_H), the high-spin state is realized.

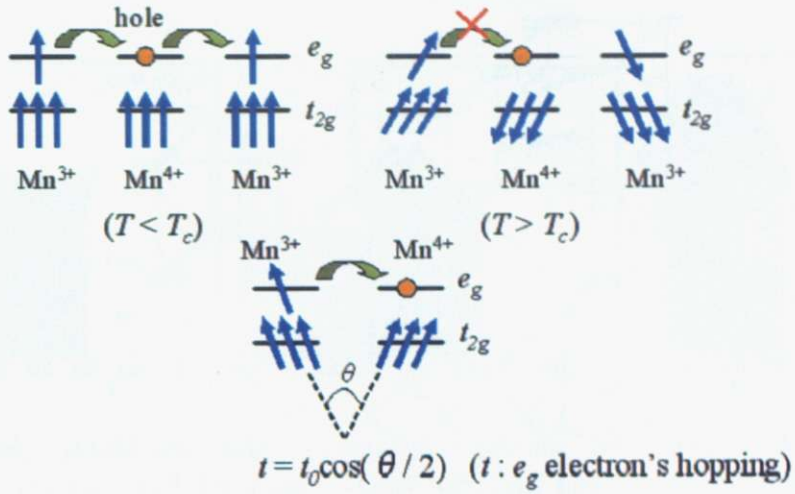

Figure 1.3: Schematic diagram of double exchange mechanism [1.9, 10].

by

$$H_{DE} = H_t + H_{\text{Hund}}, \tag{1.1}$$

$$H_t = -t \sum_{\langle ij \rangle, \sigma} (c^\dagger_{i\sigma} c_{j\sigma} + \text{H.c.}) \tag{1.2}$$

$$H_{\text{Hund}} = -J_H \sum_i \vec{S}_i \cdot \vec{\sigma}_i \tag{1.3}$$

where t is the hopping parameter of the e_g electron, J_H is ferromagnetic Hund's coupling between the e_g and t_{2g} electrons, $c^\dagger_{i\sigma}$ is a creation operator for the e_g electron with spin σ at site i, and $\vec{S}_i$ and $\vec{\sigma}_i$ represent the spin operators of the e_g and t_{2g} electrons, respectively.

The electronic phase diagrams of the typical manganites $La_{1-x}Sr_xMnO_3$, $Nd_{1-x}Sr_xMnO_3$, and $Pr_{1-x}Ca_xMnO_3$ in the temperature (T) - hole concentration (x) plane are shown in Fig. 1.4 [1.3, 5, 6, 8, 11]. As the ionic radii of the A-site ion decreases, the orthorhombic ($GdFeO_3$-type) distortion increases as shown in Fig. 1.5. As a result, the one-electron bandwidth (W) of the e_g electrons is decreased. Intermediate and small bandwidth systems such as $Nd_{1-x}Sr_xMnO_3$ and $Pr_{1-x}Ca_xMnO_3$ exhibit the so-called CE-type antiferromagnetic (AF) charge-ordered (CO) state in the doping region close to the half-doping $x = 0.5$ as shown in Fig. 1.6. The temperature dependence of magnetization, resistivity and lattice parameters in

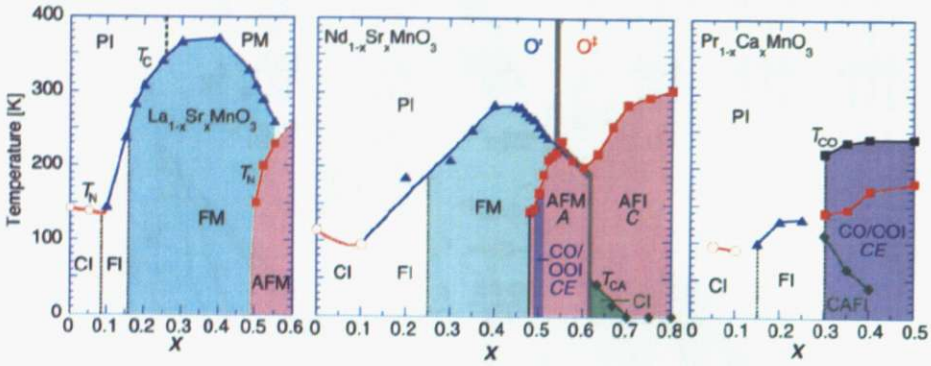

Figure 1.4: Electronic phase diagrams of $La_{1-x}Sr_xMnO_3$ (left), $Nd_{1-x}Sr_xMnO_3$ (middle) and $Pr_{1-x}Ca_xMnO_3$ (right). PI: Paramagnetic insulating; PM: Paramagnetic metallic; CI: Spin-canted insulating; FM: Ferromagnetic metallic; FI: Ferromagnetic insulating; CO/OOI: Charge-orbital ordered insulating; AFM: Antiferromagnetic metallic; AFI: Antiferromagnetic insulating; CAFI: Canted antiferromagnetic insulating (within the CO/OOI). T_C: Curie temperature; T_N: Néel temperature; T_{CO}: Charge ordering temperature; T_{CA}: Spin canting temperature [1.3, 5, 6, 8, 11]. T_C and T_{CO} denote Curie temperature and charge-ordering temperature, respectively.

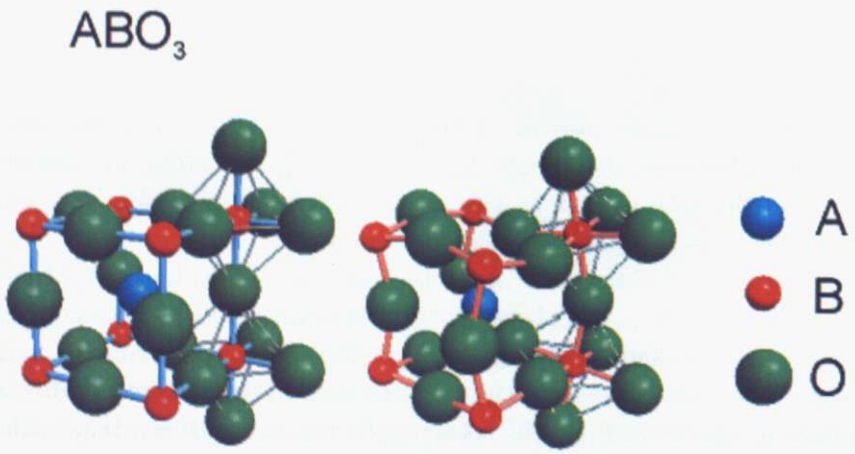

Figure 1.5: Crystal structure of perovskites ABO_3 without (left) and with the $GdFeO_3$-type distortion (right).

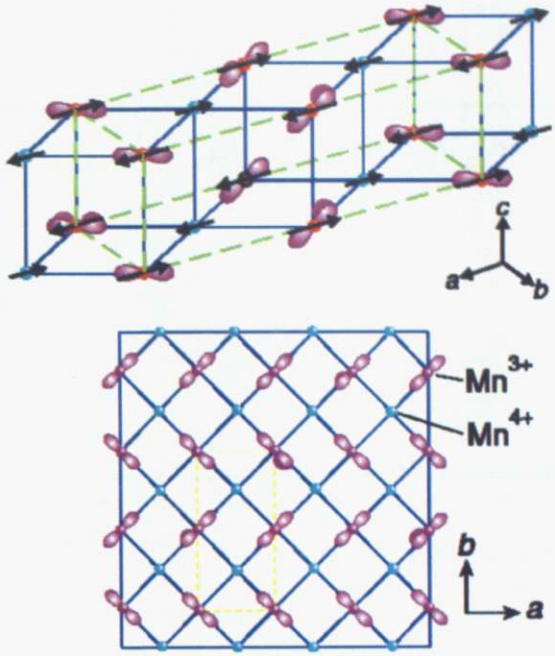

Figure 1.6: Schematic picture of the CE-type AF state including the pattern of spin, charge and orbital ordering [1.8].

NSMO ($x = 0.5$) are shown in Fig. 1.7 [1.6]. The magnetization and the resistivity in NSMO changes abruptly at the CO transition temperature (T_{CO}) [1.6]. Also, the changes of lattice parameter was observed at the T_{CO}, which suggests the ordering of e_g electrons occurs simultaneously [1.6]. In $Pr_{1-x}Ca_xMnO_3$, owing to the collapse of the CO state under the magnetic field, the CMR effect becomes remarkable as shown in Fig. 1.1 (b) [1.5]. Furthermore, $Pr_{1-x}Ca_xMnO_3$ shows an insulator-to-metal transition under an applied electric field [1.12], high pressure [1.13], irradiation of light [1.14, 15] and hard x-rays [1.16].

The coupling among spin, charge and orbital degrees of freedom is considered to be the origin of the complex phenomena in the maganites. Therefore, the DE model is insufficient to describe the large resistivity change or the entire phase diagram observed experimentally [1.17]. Many experimental and theoretical studies have unveiled the inhomogeneous character of the states of relevance to explain the CMR effect with a competition between ferromagnetic and antiferromagnetic states [1.18, 19, 20, 21, 22, 23, 24, 25, 26]. From the studies of scanning tunneling spectroscopy, the inhomogeneous structures of the metallic and insulating states were observed in

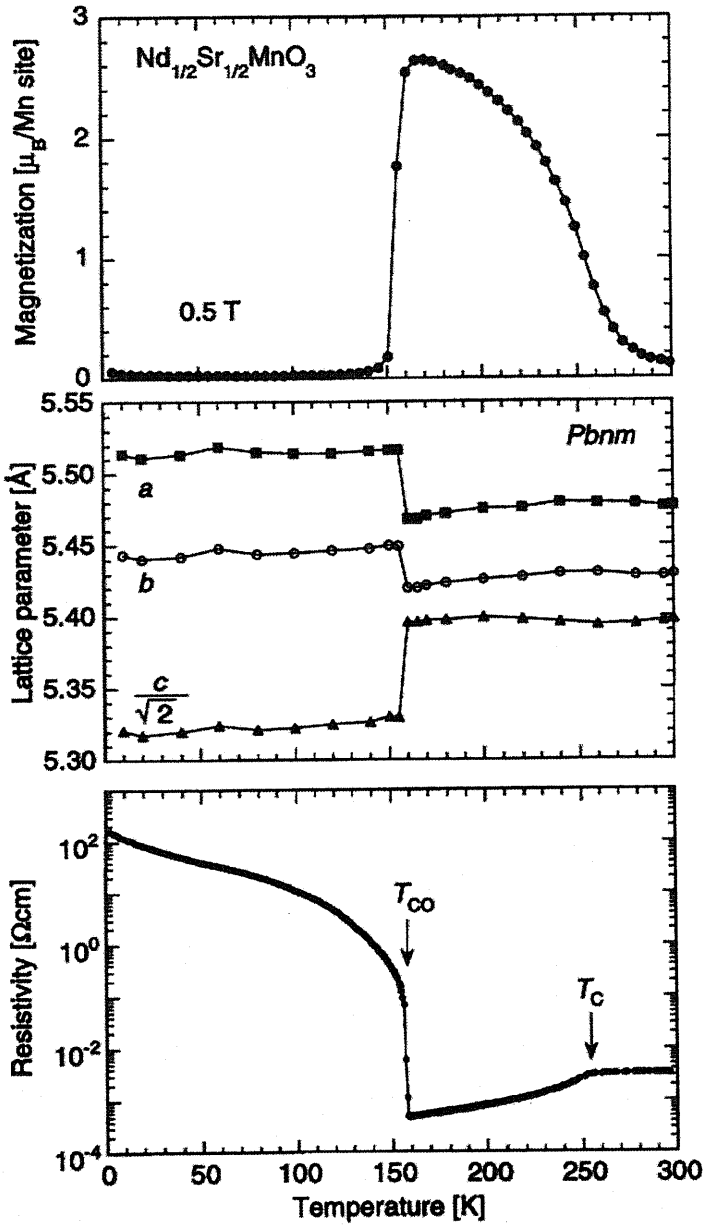

Figure 1.7: Temperature dependence of magnetization (top), resistivity (bottom) and lattice parameters (middle) in $Nd_{0.5}Sr_{0.5}MnO_3$ [1.6].

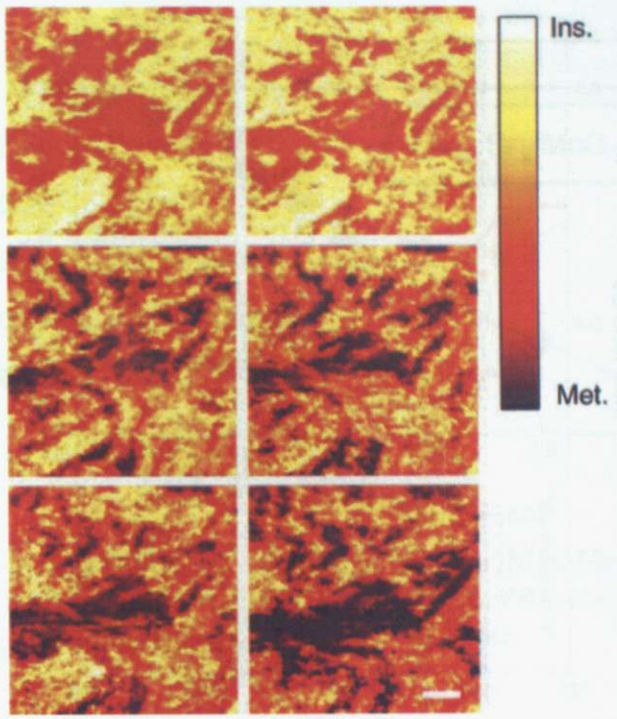

Figure 1.8: Scanning tunneling spectroscopy images of the electronic structure (metallic *vs* insulating) of $La_{1-x}Ca_xMnO_3$ thin film with $x \sim 0.3$ taken just below T_C in magnetic fields of 0, 0.3, 1, 3, 5, and 9 T (from left to right and top to bottom [1.19].

$La_{1-x}Ca_xMnO_3$ thin film with $x \sim 0.3$ as shown in Fig. 1.8 [1.19]. The cluster size and structure depend on magnetic field, which is related to a pictures of a percolative transition [1.19]. Also, a stripe formation has been observed in the CE-type CO state of manganites and a "bi-stripe" and "Wigner-crystal" model have been proposed for the stripes in $La_{1-x}Ca_xMnO_3$ and $Pr_{1-x}Ca_xMnO_3$ for $x \geq 0.5$ [1.25, 26]. The periodicity of the stripes change gradually with hole concentration and temperature as shown in Fig. 1.9 [1.27, 28, 29]. The incommensurate modulation of wave vector at high temperatures is accompanied by ferromagnetic fluctuations, probably related to the presence of the orbital disordered Mn^{3+} stripes [1.27, 28, 29].

Studies using photoemission spectroscopy are important to understand the electronic and magnetic structures of materials. From the core-level shifts of photoemission spectra, Matsuno *et al.* [1.30] have remarked that the chemical potential shift in $La_{1-x}Sr_xMnO_3$ exhibits a monotonous shift without indication of chemical potential pinning, as indicated in Fig. 1.10 [1.30].

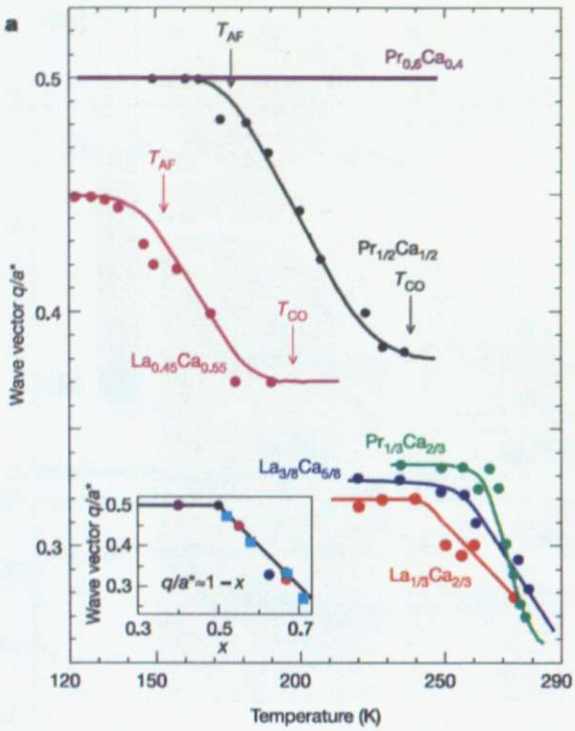

Figure 1.9: Doping and temperature dependence of the charge modulation wave vector q/a^* in $Pr_{1-x}Ca_xMnO_3$ and $La_{1-x}Ca_xMnO_3$ [1.27]. Inset shows the wave vector of the modulation versus carrier concentration at low temperatures.

This result indicates that there is no intrinsic electronic phase separation or stripe-type charge fluctuation in $La_{1-x}Sr_xMnO_3$. In spite of the smooth shift in the core levels, changes in the electronic structure of $La_{1-x}Sr_xMnO_3$ near the Fermi level (E_F) with carrier doping were highly non-rigid-band like in the sense that the Mn $3d$ e_g peak lost its intensity with hole doping while the O $1s$ x-ray-absorption intensity near E_F increases with hole doping, indicating spectral-weight transfer across E_F as shown in Fig. 1.11. [1.31, 32].

In this thesis, we present an indication of the evolution of stripe formation and competing phases as the carrier concentration, temperature, and bandwidth are varied in $Pr_{1-x}Ca_xMnO_3$, $Nd_{1-x}Sr_xMnO_3$, and $La_{1-x}Sr_xMnO_3$ investigated using photoemission spectroscopy.

The present thesis is organized as follows. The principle of photoemission spectroscopy is described in Chapter 2. The investigation of the doping and temperature dependence of chemical potential and spectral-weight

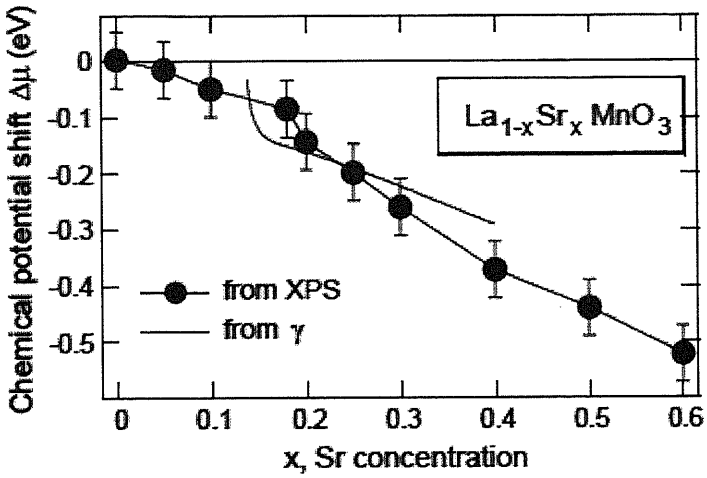

Figure 1.10: Chemical potential shift $\Delta\mu$ in $La_{1-x}Sr_xMnO_3$ as a function of the Sr concentration x. Dotted line is calculated from the electronic specific heat assuming the rigid-band model [1.30].

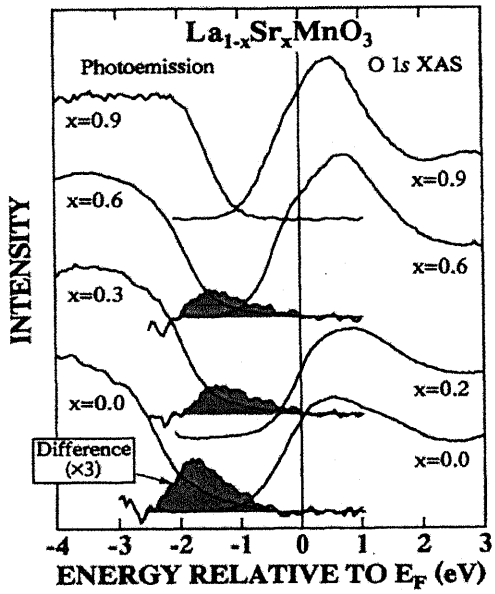

Figure 1.11: Ultraviolet-photoemission and O 1s x-ray-absorption spectra near E_F in $La_{1-x}Sr_xMnO_3$ at liquid-nitrogen temperatures [1.31]. The difference spectra relative to $x = 0.9$ are also shown.

transfer near E_F in $Pr_{1-x}Ca_xMnO_3$ is discussed in Chapters 3, and 4, respectively. The study of doping and temperature-dependent chemical potential shift in $Nd_{1-x}Sr_xMnO_3$ is presented in Chapters 5 and 6. We describe the summary of the chemical potential shift with carrier concentration and also discuss the shift induced by band-width control in manganites in Chapter 7. Chapter 8 focuses on the photoinduced effects in $Pr_{1-x}Ca_xMnO_3$ and $Nd_{1-x}Sr_xMnO_3$. Finally, we summarize our results and draw conclusions.

References

[1.1] M. Imada, A. Fujimori, and Y. Tokura, Rev. Mod. Phys. **70**, 1039 (1998).

[1.2] J. B. Bednorz, and K. A. Müller, Z. Phys. B **64**, 189 (1986).

[1.3] A. Urushibara, Y. Moritomo, T. Arima, A. Asamitsu, G. Kido, and Y. Tokura, Phys. Rev. B **51**, 14103 (1995).

[1.4] Y. Tokura, A. Urushibara, Y. Moritomo, T. Arima, A. Asamitsu, G. Kido, and N. Furukawa, J. Phys. Soc. Jpn. **63**, 3931 (1994).

[1.5] Y. Tomioka, A. Asamitsu, H. Kuwahara, Y. Moritomo, and Y. Tokura, Phys. Rev. B **53**, 1689 (1996).

[1.6] H. Kuwahara, Y. Tomioka, A. Asamitsu, Y. Moritomo, and Y. Tokura, Science **270**, 961 (1995).

[1.7] Y. Tokura and N. Nagaosa, Science **288**, 462 (2000).

[1.8] Y. Tokura, Rep. Prog. Phys **69**, 797 (2006).

[1.9] C. Zener, Phys. Rev. **82**, 403 (1951).

[1.10] P. W. Anderson and H. Hasegawa, Phys. Rev. **100**, 675 (1955).

[1.11] Y. Tokura and Y. Tomioka, J. Magn. Magn. Mater **200**, 1 (1999).

[1.12] A. Asamitsu, Y. Tomioka, H. Kuwahara, and Y. Tokura, Nature **388**, 50 (1997).

[1.13] Y. Moritomo, H. Kuwahara, Y. Tomioka, and Y. Tokura, Phys. Rev. B **55**, 7549 (1997).

[1.14] K. Miyano, T. Tanaka, Y. Tomioka, and Y. Tokura, Phys. Rev. Lett. **78**, 4257 (1997).

[1.15] M. Fiebig, K. Miyano, Y. Tomioka, and Y. Tokura, Science **280**, 1925 (1998).

[1.16] V. Kiryukhin, D. Casa, J. P. Hill, B. Keimer, A. Vigliante, Y. Tomioka, and Y. Tokura, Nature **386**, 813 (1997).

[1.17] A. J. Millis, B. I. Shraiman, and R. Mueller, Phys. Rev. Lett. **77**, 175 (1996).

[1.18] E. Dagotto, T. Hotta, and A. Moreo, Physics Reports **344**, 1 (2001).

[1.19] M. Fäth, S. Freisem, A. A. Menovsky, Y. Tomioka, J. Aarts, and J. A. Mydosh, Science **285**, 1540 (1999).

[1.20] S. Mori, C. H. Chen, and S.-W. Cheong, Phys. Rev. Lett. **81**, 3972 (1998).

[1.21] M. Uehara, S. Mori, C. H. Chen, and S.-W. Cheong, Nature **399**, 560 (1999).

[1.22] D. D. Sarma, D. Topwal, U. Manju, S. R. Krishnakumar, M. Bertolo, S. L. Rosa, G. Cautero, T. Y. Koo, P. A. Sharma, S.-W. Cheong, and A. Fujimori, Phys. Rev. Lett. **93**, 097202 (2004).

[1.23] S. Yunoki, J. Hu, A. L. Malvezzi, A. Moreo, N. Furukawa, and E. Dagotto, Phys. Rev. Lett. **80**, 845 (1998).

[1.24] A. Moreo, S. Yunoki, and E. Dagotto, Science **283**, 2034 (1999).

[1.25] S. Mori, C. H. Chen, and S.-W. Cheong, Nature **392**, 473 (1998).

[1.26] P. G. Radaelli, D. E. Cox, L. Capogna, S.-W. Cheong, and M. Marezio, Phys. Rev. B **59**, 14440 (1999).

[1.27] G. C. Milward, M. J. Calderon, and P. B. Littlewood, Nature **433**, 607 (2005).

[1.28] C. H. Chen, S. Mori, and S.-W. Cheong, Phys. Rev. Lett. **83**, 4792 (1999).

[1.29] S. Mori, T. Katsufuji, N. Yamamoto, C. H. Chen, and S.-W. Cheong, Phys. Rev. B **59**, 13573 (1999).

[1.30] J. Matsuno, A. Fujimori, Y. Takeda, and M. Takano, Europhys. Lett. **59**, 252 (2002).

[1.31] T. Saitoh, A. E. Bocquet, T. Mizokawa, H. Namatame, A. Fujimori, M. Abbate, Y. Takeda, and M. Takano, Phys. Rev. B **51**, 13942 (1995).

[1.32] K. Horiba, A. Chikamatsu, H. Kumigashira, M. Oshima, N. Nakagawa, M. Lippmaa, K. Ono, M. Kawasaki, and H. Koinuma, Phys. Rev. B **71**, 155420 (2005).

Chapter 2

Experimental methods

2.1 Principle of photoemission spectroscopy

2.1.1 General formulation

Photoemission spectroscopy (PES) is a powerful technique to investigate the electronic structure of materials directly. In this section, I briefly present the principle of PES.

When the incident photon with the kinetic energy $h\nu$ hits the sample, a photoelectron is emitted from the sample via the photoelectronic effect. In this process, the energy conservation rule holes:

$$E_{kin}^{vac} = h\nu - \Phi - E_B, \tag{2.1}$$

where E_{kin}^{vac} is the kinetic energy measured relative to the vacuum level E_{vac}, Φ is the work function of the sample, and E_B is the binding energy measured relative to the Fermi level E_F. The schematic picture of this process is displayed in Fig. 2.1. For incident photon energy, therefore, one can obtain photoemission spectra by counting the number of photoelectrons as a function of kinetic energy E_{kin}^{vac}. In real experiments, however, the kinetic energy (E_{kin}) measured relative to the Fermi level

$$E_{kin} = h\nu - E_B \tag{2.2}$$

is directly observed rather than E_{kin}^{vac}.

In the one-electron approximation, the obtained spectrum gives the density of states (DOS) of the band electrons and the binding energy can be expressed as:

$$E_B = -\epsilon_k, \tag{2.3}$$

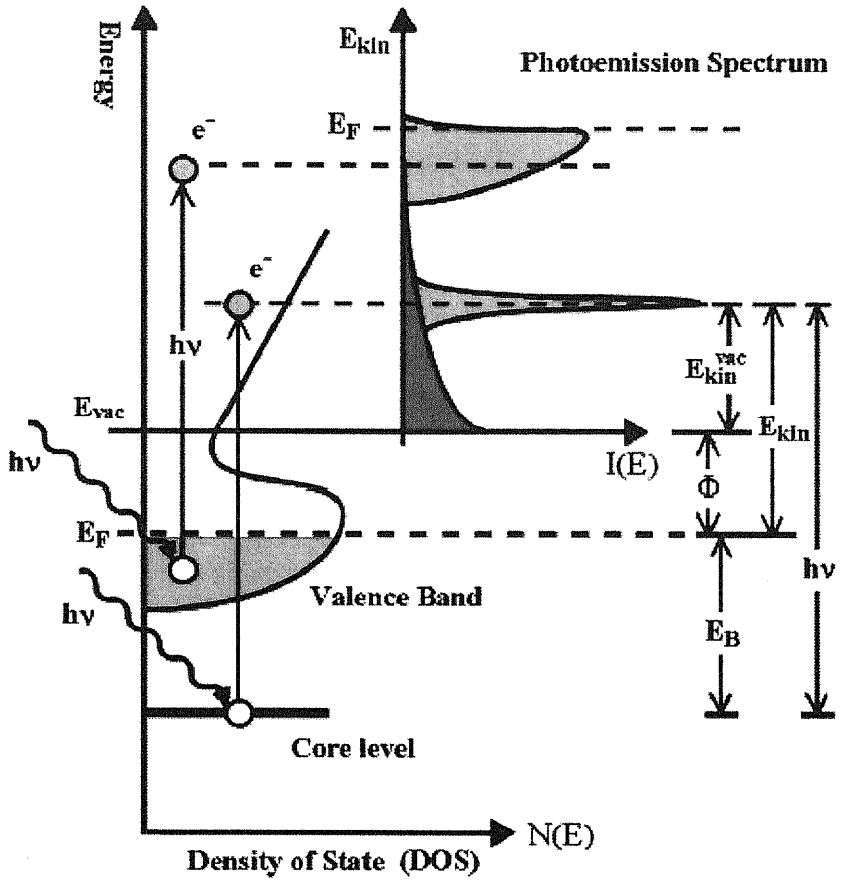

Figure 2.1: Schematic diagram of the principle of photoemission spectroscopy.

here, ϵ_k is the Hartree-Fock energy of orbital k called *Koopmans' orbital energy* [2.1]. If one can apply this approximation, the photoemission spectrum $I(E_B)$ is given by

$$I(E_B) \propto \sum_k \delta(E_B + \epsilon_k) \propto N(-E_B), \tag{2.4}$$

where $N(E)$ is the DOS of the occupied one-electron states. Thus, when the one-electron approximation is valid, the photoemission spectrum is proportional to the DOS $N(E)$ (Fig. 2.1).

Next, let us take many-electron effects into account beyond the one-electron approximation. In this more generalized description, photoemission process is regarded as the removal of an electron from the ground state $|\Psi_0^N\rangle$

of the N-electron system with energy E_0^N, leaving the system in an excited state $|\Psi_n^{N-1}\rangle$ of the $(N-1)$-electron system with energy E_n^{N-1}. Then, E_B gives the difference between E_0^N and E_n^{N-1} namely,

$$E_B = E_n^{N-1} - E_0^N + \mu. \tag{2.5}$$

Using Fermi's golden rule, the photoemission spectrum, which now corresponds to the single-particle excitation spectrum of the system, is expressed as

$$I(\omega) \propto \sum_{k,n} |\langle \Psi_n^{N-1}|c_k|\Psi_0^N\rangle|^2 \delta(\omega + E_n^{N-1} - E_0^N), \tag{2.6}$$

where c_k is the annihilation operator of the electron with the momentum k. Let the Green's function $G(k,t)$ defined as

$$G(k,t) \equiv -i\theta(t)\langle \Psi_0^N|\{c_k(t), c_k^\dagger\}|\Psi_0^N\rangle, \tag{2.7}$$

where $c_k^\dagger$ is the creation operator of an electron with the momentum k and $c_k(t) \equiv e^{iHt}c_k e^{-iHt}$. The Fourier's transform of $G(k,t)$ is given by

$$\begin{aligned} G(k,\omega) &= -i\int_0^\infty dt \langle \Psi_0^N|\{c_k(t), c_k^\dagger\}|\Psi_0^N\rangle e^{i\omega t - \epsilon t} \\ &= \langle \Psi_0^N|c_k^\dagger \frac{1}{\omega + i\epsilon + H - E_0^N} c_k|\Psi_0^N\rangle + \langle \Psi_0^N|c_k \frac{1}{\omega + i\epsilon - H + E_0^N} c_k^\dagger|\Psi_0^N\rangle \\ &= \sum_n |\langle \Psi_n^{N-1}|c_k|\Psi_0^N\rangle|^2 [\frac{P}{\omega + E_n^{N-1} - E_0^N} - i\pi\delta(\omega + E_n^{N-1} - E_0^N)] \\ &+ \sum_n |\langle \Psi_n^{N+1}|c_k^\dagger|\Psi_0^N\rangle|^2 [\frac{P}{\omega - E_n^{N+1} + E_0^N} - i\pi\delta(\omega - E_n^{N+1} + E_0^N)], \end{aligned} \tag{2.8}$$

where H is the Hamiltonian of the system and P denotes the principal value of an integral.

The spectral function $A(k,\omega)$ is given by

$$\begin{aligned} A(k,\omega) &= -\frac{1}{\pi}\mathrm{Im}G(k,\omega) \\ &= \sum_n |\langle \Psi_n^{N-1}|c_k^\dagger|\Psi_0^N\rangle|^2 \delta(\omega + E_n^{N-1} - E_0^N) \quad \text{for } \omega \le \mu. \end{aligned} \tag{2.9}$$

Finally, one obtains

$$I(\omega) \propto -\frac{1}{\pi}\sum_k \mathrm{Im}G(k,\omega) \quad \text{for } \omega \le \mu. \tag{2.10}$$

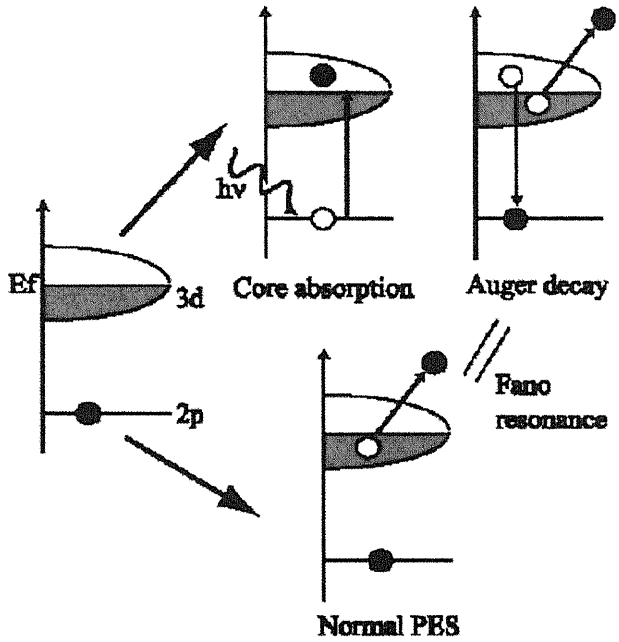

Figure 2.2: Schematic diagram of resonant photoemission spectroscopy.

It must be emphasized that the information about final states which is obtained in the PES measurements does not necessarily reflect the one-electron DOS for strongly correlated electron systems. Therefore, the interpretation of the spectra becomes complicated, but one can obtain information about electron correlation effects by analyzing the spectra.

2.1.2 Resonant photoemission spectroscopy

Using resonant photoemission spectroscopy, one can selectively modulate the direct $3d$-electron emission in a valence-band photoemission spectra of a transition-metal oxides. A schematic diagram of resonant photoemission spectroscopy is depicted in Fig. 2.2. When the energy of the incident photon is equal to the energy difference between the p core level and the valence d states, besides the direct photoemission process of a valence d electron,

$$p^6 d^N + h\nu \rightarrow p^6 d^{N-1} + e^-,$$

the photoabsorption and subsequent Auger-type decay, called super Coster-Krönig decay,

$$p^6 d^N + h\nu \rightarrow p^5 d^{N+1} \rightarrow p^6 d^{N-1} + e^-,$$

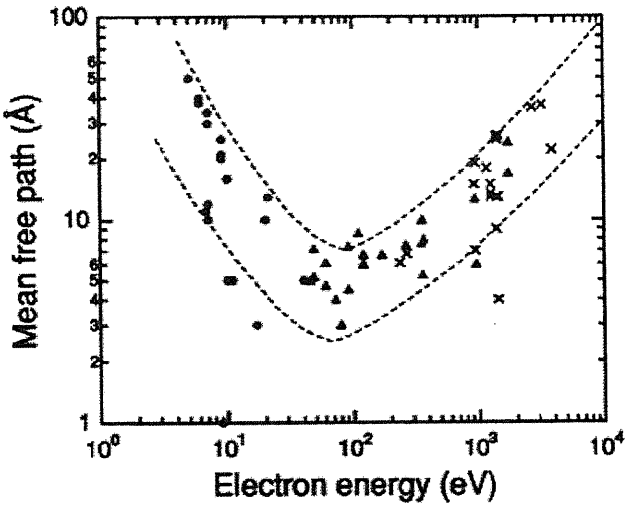

Figure 2.3: Mean-free path of electrons in solids as a function of electron energy. Dashed curves indicate the approximate range of distribution [2.3, 4].

occur. Both the initial and the final states of these two processes have the same electron configurations, and therefore a quantum-mechanical interference occurs. The photoemission intensity is resonantly enhanced and shows a so-called Fano profile [2.2]. Since this enhancement takes place only for the emission of d electrons, one can obtain the d partial DOS in the compounds.

2.1.3 Electron escape depth

Photoemission spectroscopy is a fairly surface sensitive technique. The escape depth of the electrons is determined by electron-electron and electron-phonon collisions. Except for special cases, electron-phonon scattering plays a role only at low energies below the phonon frequencies. The escape depth of the electron λ is determined then largely by electron-electron interaction. The cross-section for electron-electron scattering σ is given by

$$\frac{d\sigma}{d\Omega d\omega} \propto \frac{1}{q^2}\mathrm{Im}\left[-\frac{1}{\varepsilon(q,\omega)}\right], \tag{2.11}$$

where $\varepsilon(q,\omega)$ is the dielectric function, q is the momentum and ω is the energy of the electron. Thus λ^{-1} is essentially determined by $\varepsilon(q,\omega)$. In principle, since the dielectric function is specific to the material, the escape depth is specific to each material. However, except for small energies ($\lesssim$ 10 eV), the electron in solids can be approximately described by a free-electron gas because the bonding properties are no longer important. In this

case, the plasma frequency which is a function of only the valence electron density or the mean electron-electron distance r_s determines the loss function $\mathrm{Im}\{-1/\varepsilon\}$. Then, the inverse escape depth λ^{-1} is described by the mean electron-electron distance r_s which is roughly equal for all materials, and one obtains

$$\lambda^{-1} \simeq \sqrt{3}\frac{a_0 R}{E_{kin}} r_s^{-3/2} \log\left[\left(\frac{4}{9\pi}\right)^{2/3} \frac{E_{kin}}{R} r_s^2\right], \tag{2.12}$$

where $a_0 = 0.529$ Å, $R = 13.6$ eV, and r_s is measured in units of Bohr radius a_0. This gives us the escape depth as a function of photoelectron kinetic energy E_{kin}, which is called "universal curve" as has been measured experimentally as shown in Fig. 2.3.

2.2 Photoemission measurement system

Photoemission measurements were carried out using a hemispherical analyzer (GAMMADATA-SCIENTA SES-100). Figure 2.4 shows a schematic description of the photoemission measurment system. In the ultra-high vacuum chamber, elecrons in the solid sample are excited by incident photons. The emitted photoelectrons enter the electron lens and are focused by electrostatic fields. The photoelectrons are deaccelerated by a retarding potential V_R before entering the electron analyzer. The analyzer transmits only photoelectrons with a given energy (pass energy E_P). The relationship between the retarding potential V_R and the pass energy E_P is given by

$$E_P = E_{kin} - eV_R - \phi_A, \tag{2.13}$$

where ϕ_A is the work function of the analyzer (Fig. 2.5).

One can sweep E_{kin} by sweeping E_P or V_R. The energy resolution of the electron analyzer ΔE is expressed as

$$\Delta E = E_P\left(\frac{w}{2R_0} + \frac{\alpha^2}{4}\right), \tag{2.14}$$

where w is the silt width, R_0 is the mean radius of the hemispheres, and α is the acceptance angle of the entrance slit. In experiments E_P is usually kept constant and V_R is swept so that ΔE is kept constant independent of E_{kin}.

Previously, channeltrons were widely used as an electron detector. However, to improve the detection efficiency of photoelectrons in the single-channeltron system, E_P or w must be made larger, making ΔE worse according to Eq. (2.14). To improve the detection efficiency with keeping ΔE,

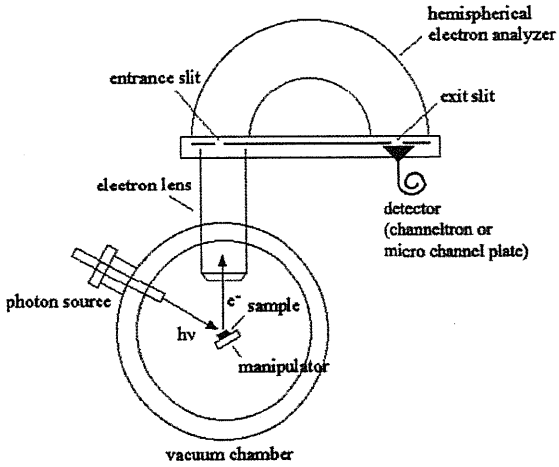

Figure 2.4: Schematic description of the photoemission measurement system.

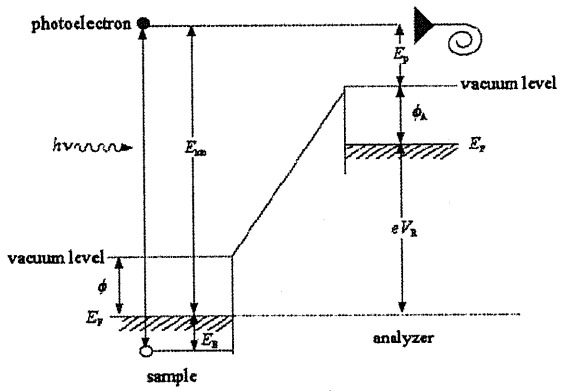

Figure 2.5: Diagram showing potentials and energy levels for the sample and the analyzer. Relationship between E_P and V_R can be seen.

a multi-channel detection system with a micro-channel plate (MCP) has been used recently. SCIENTA SES-100 also uses an MCP as a detector. Each channel detects photoelectrons which went through different passes in the analyzer, meaning that each channel detects electrons with different pass energies. By calibrating this difference, one can improve the detection efficiency without making ΔE worse.

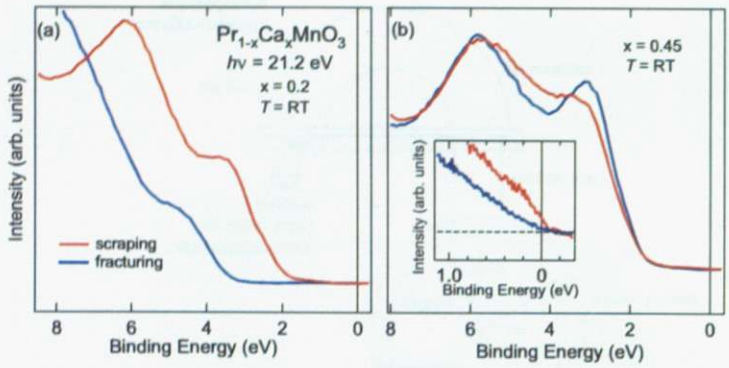

Figure 2.6: Comparison between the valence-band photoemission spectra of scraped and fractured bulk crystals of $Pr_{1-x}Ca_xMnO_3$ at room temperature taken at $h\nu = 21.2$ eV. (a) $x = 0.2$; (b) $x = 0.45$.

2.3 Surface preparation for ultraviolet photoemission spectroscopy

Since the measurements of ultraviolet photoemission spectroscopy (UPS) are surface sensitive due to the short mean-free path of the low-energy photoelectron, spectral weight near Fermi level (E_F) strongly depends on the surface preparations (scraping or fracturing). Figure 2.6 shows comparison between the UPS spectra of scraped and fractured bulk crystals in $Pr_{1-x}Ca_xMnO_3$ with $x = 0.2$ and 0.45 at room temperature. For $x = 0.2$, charging effect, which causes an energy shift towards higher binding energies, occurred in the fractured sample, but not in the scraped one. The fractured sample surfaces may be affected by lattice defect, contamination/degradation-related features, and so on because $Pr_{1-x}Ca_xMnO_3$ does not have a cleavage plane. Also, for $x = 0.45$, the valence-band structures are sharp, but the spectral weight near E_F was considerably suppressed in the fractured sample. It is likely that angle-resolved electrons are detected for the fractured sample. Therefore, we applied the scraping to the $Pr_{1-x}Ca_xMnO_3$ samples and confirmed that the valence-band spectra did not change with further scrapings.

2.4 Chemical potential shift

In order to deduce the chemical potential shift from a set of core-level data, we utilize the formula [2.4, 5] that the shift ΔE_B of the binding energy is given by $\Delta E_B = \Delta\mu + K\Delta Q + \Delta V_M - \Delta E_R$, where $\Delta\mu$ is the change

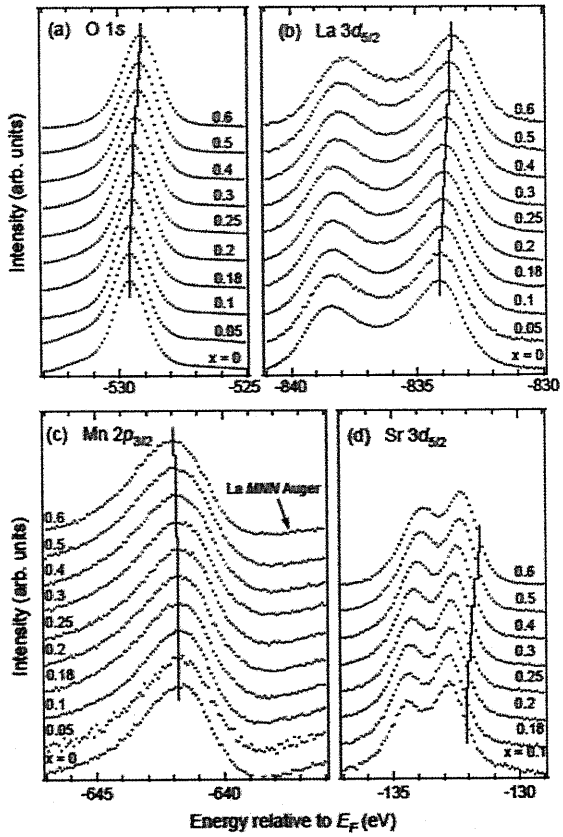

Figure 2.7: Core-level photoemission spectra of $La_{1-x}Sr_xMnO_3$ taken with the Mg $K\alpha$ line. (a) O $1s$; (b) La $3d$; (c) Mn $2p$; (d) Sr $3d$. [2.6]. Energies are referenced to the chemical potential μ.

in the chemical potential, K is the coupling constant of the Coulomb interaction between the valence and core electrons, ΔQ is the change in the number of valence electrons on the atom considered, ΔV_M is the change in the Madelung potential, and ΔE_R is the change in the extra-atomic relaxation energy. Here, ΔQ produces changes in the electrostatic potential at the core-hole site as well as in the intra-atomic relaxation energy of the core-hole final state. ΔE_R is due to changes in the screening of the core-hole potential by metallic-conduction electrons and polarizable surrounding ions.

Figure 2.7 shows the photoemission spectra of the O $1s$, La $3d$, Mn $2p$ and Sr $3d$ core levels taken at Mg $K\alpha$ source ($h\nu$ = 1253.6 eV) [2.6]. The vertical lines mark the estimated positions of the core levels whose line shapes do not change significantly with composition. Figure 2.8 shows the

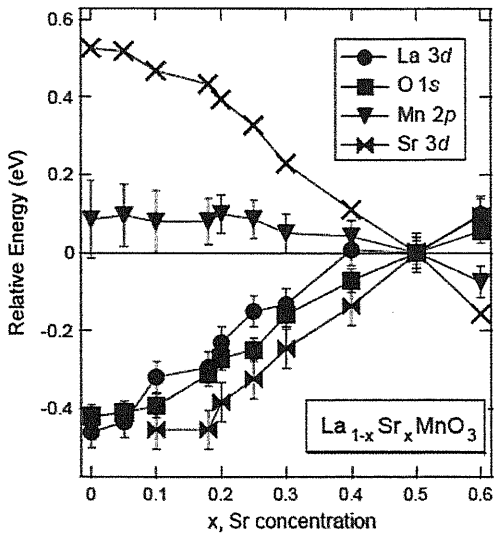

Figure 2.8: Energy shifts of the O $1s$, La $3d$, Mn $2p$ and Sr $3d$ core levels relative to $x = 0.5$ as functions of carrier concentration x [2.6]. Crosses denote the diffence between the shift of the Mn $2p$ core level and the average shift of the the O $1s$, La $3d$ and Sr $3d$ core levels.

energy shifts of each core level as a function of hole concentration x [2.6]. One can see that the observed energy shifts with x were approximately common to the O $1s$, Sr $3d$, and La $3d$ core levels, while the Mn $2p$ core level moves in the opposite direction. Core-hole screening by conduction electrons can be excluded from the main origin of the core-level shifts [2.7, 8]. The change in the Madelung potential has also negligible effects on the core-level shifts because the identical core-level shifts of the O^{2-} anion and the Sr^{2+} and La^{3+} cations were observed [2.6]. Therefore, we assume that $\Delta E_B \simeq \Delta\mu + K\Delta Q$. The chemical-shift term is important for the Mn $2p$ core-level shift because of the increase in the Mn valence with hole doping ($\propto -\Delta Q$) from Mn^{3+} towards Mn^{4+}, i.e., because of the so-called chemical shift. Therefore, it is considered that the shifts of the O $1s$, Sr $3d$, and La $3d$ core levels are largely due to the chemical potential shift $\Delta\mu$, and one can estimate the $\Delta\mu$ in LSMO by taking the average of the shifts of the three core levels as shown in Fig. 1.10 [2.6].

References

[2.1] T. A. Koopmans, Physica **1**, 104 (1933).

[2.2] U. Fano, Phys. Rev. **124**, 1866 (1961).

[2.3] C. R. Brundle, J. Vac. Sci. Technol. **11**, 212 (1974).

[2.4] S. Hüfner, *Photoelectron Spectroscopy* (Springer-Verlag, Berlin, 2003).

[2.5] A. Fujimori, A. Ino, J. Matsuno, T. Yoshida, K. Tanaka, and T. Mizokawa, J. Electron Spectrosc. Relat. Phenom. **124**, 127 (2002).

[2.6] J. Matsuno, A. Fujimori, Y. Takeda, and M. Takano, Europhys. Lett. **59**, 252 (2002).

[2.7] A. Ino, T. Mizokawa, A. Fujimori, K. Tamasaku, H. Eisaki, S. Uchida, T. Kimura, T. Sasagawa, and K. Kishio, Phys. Rev. Lett. **79**, 2101 (1997).

[2.8] N. Harima, J. Matsuno, A. Fujimori, Y. Onose, Y. Taguchi, and Y. Tokura, Phys. Rev. B **64**, 220507(R) (2001).

Chapter 3

Doping dependence of chemical potential and spectral-weight transfer in $Pr_{1-x}Ca_xMnO_3$

Part of this chapter has been published in

- "Chemical potential shift and spectral-weight transfer in $Pr_{1-x}Ca_xMnO_3$ revealed by photoemission spectroscopy" by K. Ebata, H. Wadati, M. Takizawa, A. Fujimori, A. Chikamatsu, H. Kumigashira, M. Oshima, Y. Tomioka, and Y. Tokura, Phys. Rev. B **74**, 064419 (2006).
- "Photoemission Study of Perovskite-type Manganites with Stripe Ordering" by K. Ebata, H. Wadati, M. Takizawa, K. Maekawa, A. Fujimori, A. Chikamatsu, H. Kumigashira, M. Oshima, Y. Tomioka, H. Kuwahara, and Y. Tokura, J. Supercond. Nov. Magn. **20**, 543-546 (2007).

3.1 Introduction

Half-doped manganites ($x \simeq 0.5$) have been a focus of recent studies because most of them exhibit a so-called charge exchange (CE)-type antiferromagnetic (AF) charge-ordered (CO) state. The compound $Pr_{1-x}Ca_xMnO_3$ (PCMO), in which the bandwidth W is small in comparison with other manganites, has a particularly stable CO state over the wide hole concentration region between $x \simeq 0.3$ and 0.75 as shown in the electronic phase diagram in Fig. 3.1 [3.1, 2, 3]. Furthermore, CMR in the CO state of PCMO has been found remarkable, amounting to several orders of magnitude [3.2].

The origin of the CMR effect has been debated in recent years since it was pointed out that DE mechanism alone was insufficient to explain the

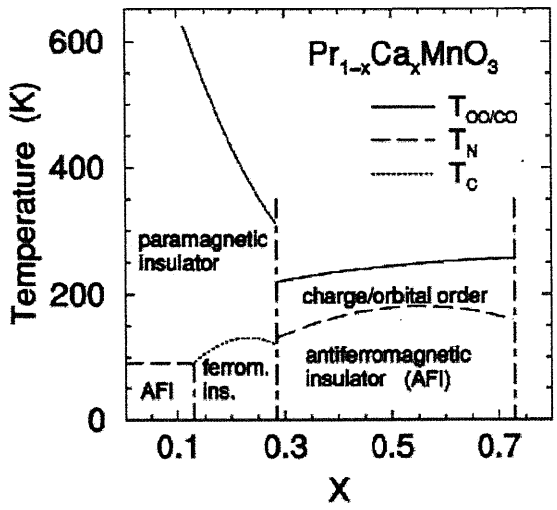

Figure 3.1: Electronic phase diagram of $Pr_{1-x}Ca_xMnO_3$ [3.1, 2, 3].

large resistivity change with magnetization [3.4]. Recently, the possibility of charge self-organization such as phase separation (PS) as the origin of the CMR effect has been discussed in theoretical and experimental studies. In computational work based on quantum Monte Carlo simulation, the possibility of PS into the ferromagnetic (FM) and AF phases has been pointed out [3.5, 6]. The calculated density of electrons $\langle n \rangle$ versus chemical potential μ for a one-dimensional model has shown a clear discontinuity in $\langle n \rangle$ at a particular value of μ as shown in Fig. 3.2, indicating a PS [3.5, 6] since in general electronic PS results in the pinning of μ. Indeed, electron microscopy studies have revealed inhomogeneous spatial images in which the FM charge-disordered and AF CO microdomains coexist [3.7, 8, 9]. However, it has been unclear whether they are driven by (intrinsic) tendency toward electronic PS or triggered by (extrinsic) chemical inhomogenity. Electronic "PS" on a nano-meter scale such as stripe formation would also lead to the pinning of the chemical potential, in analogy to the case of high-T_c cuprates [3.10]. It has also been shown theoretically that the introduction of chemical disorder turns the chemical potential pinning into a smooth shift as shown in Fig. 3.3 [3.11]. Therefore, one can distinguish intrinsic electronic inhomogenity from extrinsic chemical disorder through the measurements of chemical potential shift.

The chemical potential shift can be deduced from the core-level shifts of photoemission spectra as functions of carrier concentration. Recently, it has been shown that the chemical potential shift in $La_{1-x}Sr_xMnO_3$ (LSMO),

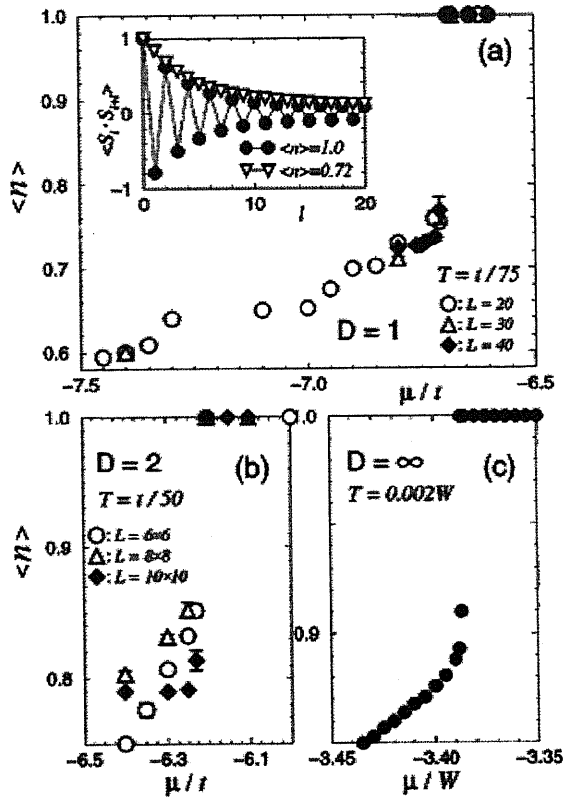

Figure 3.2: Density of e_g electrons $\langle n \rangle$ *vs.* chemical potential μ for clusters with (a) $D = 1$, (b) $D = 2$, (c) $D = \infty$, where D is the spatial dimension, t is the hopping parameter and W is the half-width of the density of states [3.5].

which has the widest bandwidth among the manganites, shows a monotonous shift without indication of chemical potential pinning, especially around $x \simeq 0.3$, where the CMR effect is the strongest [3.12]. It has therefore been considered that there is no intrinsic electronic "PS" in LSMO.

In this chapter, we report on a core-level photoemission study of the chemical potential shift ($\Delta\mu$) as a function of carrier concentration and the composition dependence of the valence-band spectra in single crystals of PCMO. The results show that the chemical potential pinning occurs due to the change of periodicity of stripes, spectral weight is transferred toward near Fermi level (E_F) with hole doping, and there is a finite intensity at E_F in the paramagnetic insulating (PI) phase on the high temperature side of the CO transition temperature for $x \gtrsim 0.3$.

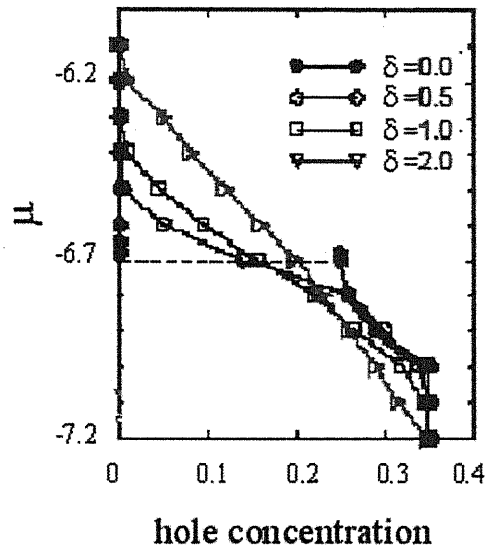

Figure 3.3: Results of quantum Monte Carlo simulation with a disorder effect. δ is the magnitude of disorder potential in units of t [3.11].

3.2 Experimental

Single crystals of PCMO with the carrier concentrations of $x = 0.2$, 0.25, 0.3, 0.35, 0.4, 0.45, 0.5, 0.6, and 0.65 were grown by the floating-zone method. These samples were supplied by Dr. Y. Tomioka and Prof. Y. Tokura of National Institute of Advanced Industrial Science and Technology. The crystal growth was performed in a 100 % O_2 atmosphere at a rate of 3-5 mm/h with rotation of the seed and feed rods in opposite directions. The middle part of the rod was cut out and characterized by the x-ray Laue and neutron-diffraction measurements, which confirmed the formation of single crystals. The x-ray powder analysis indicated that the samples were in a single phase with the orthorhombically distorted perovskite lattice. The orthorhombic distortion was observed to decrease with x. The electron-probe microanalysis (EPMA) indicated a nearly identical composition with a prescribed one for each crystal [3.2]. The temperature dependence of the electrical resistivity (ρ-T curve) for PCMO crystals in the absence of a magnetic field and under magnetic fields are shown in Fig. 3.4 [3.2]. The photoemission spectroscopy (PES) measurements using synchrotron radiation were performed at BL-2C of Photon Factory, High Energy Acceleration Research Organization (KEK). We carried out the measurements using the photon energies of $h\nu$ = 600 eV, 643.6 eV (Mn 2p-3d resonance), 800 eV, and 930 eV (Pr

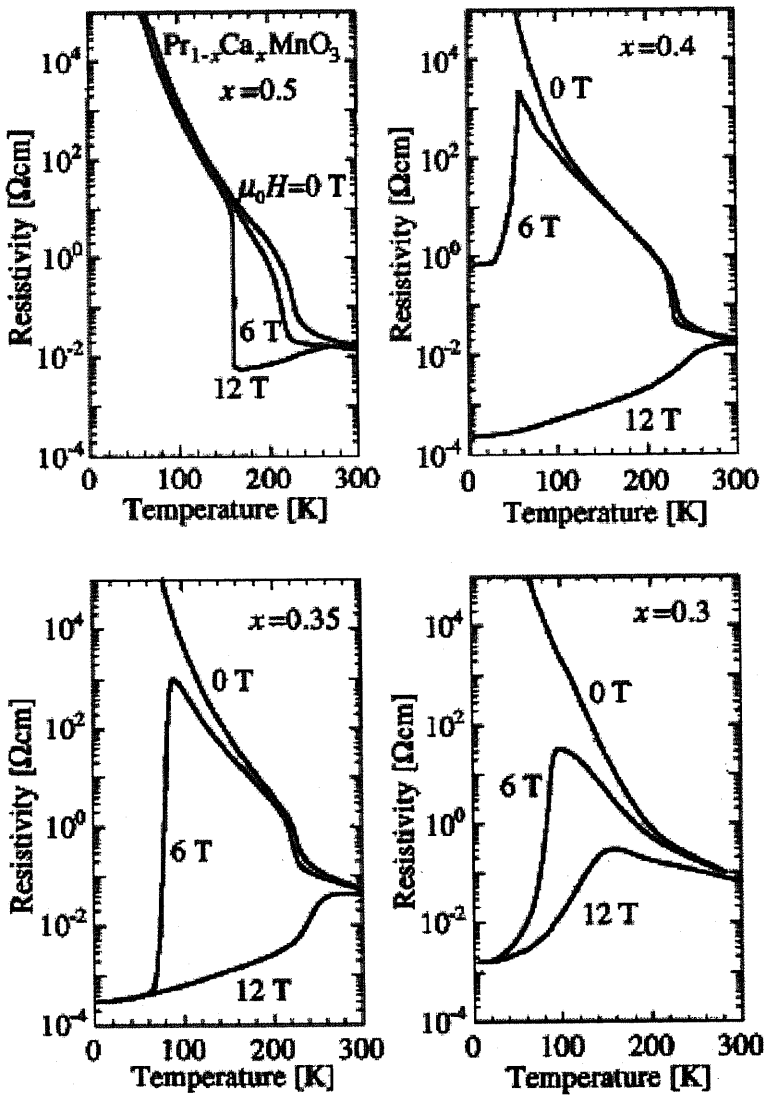

Figure 3.4: Temperature dependence of the resistivity (ρ-T curve) under H = 0, 6, and 12 T for $Pr_{1-x}Ca_xMnO_3$ [3.2].

$3d$-$4f$ resonance). Ultraviolet photoemission spectroscopy (UPS) and X-ray photoemission spectroscopy (XPS) measurements were also performed using the photon energies of $h\nu = 21.2$ eV (He I) and 1253.6 eV (Mg $K\alpha$). All the photoemission measurements were performed under the base pressure of $\sim 10^{-10}$ Torr at 80 K and room temperature (RT). The samples were repeatedly scraped *in situ* with a diamond file to obtain clean surfaces. In the case of PES using synchrotron radiation and XPS, the cleanliness of the sample surface was checked by the reduction of the shoulder on the high binding energy side of the O $1s$ core level. In the case of UPS, the scraping was made until a bump around 9-10 eV, which is attributed to surface contamination, decreased and the valence-band spectra did not change with further scrapings. Photoelectrons were collected using a Scienta SES-100 electron-energy analyzer. The energy resolution was about 200-500 meV for the synchrotron radiation measurements, 20 meV for He I, and 800 meV for Mg $K\alpha$. The measured binding energies were stable, judged from the fact the gold $4f_{7/2}$ core-level spectrum was nearly unchanged throughout the measurements.

3.3 Results and discussion

3.3.1 Chemical potential shift

3.3.1.1 Low-temperature CE-type charge-ordered phase

Figure 3.5 shows the photoemission spectra of the O $1s$, Ca $2p$, Pr $3d$, and Mn $2p$ core levels at 80 K. For the O $1s$ core level, we have used the midpoint of the low binding-energy slope because the line shape on the higher binding energy side of the O $1s$ spectra is known to be sensitive to surface contamination or degradation. We have also used the midpoint for the Ca $2p$ and Mn $2p$ core levels. As for the Pr $3d$ core level, 80 % of the peak height of the low binding-energy slope was used because the line shape near the midpoint on the lower-binding energy side slightly changed with hole concentration.

In Fig. 3.6(a), the binding energy shifts of the O $1s$, Ca $2p$, Pr $3d$, and Mn $2p$ core levels at 80 K are plotted. One can see from Fig. 3.6(a) that the observed binding energy shifts with x were approximately common to the O $1s$, Ca $2p$, and Pr $3d$ core levels, whereas the shift of the Mn $2p$ core level was different from them. The similar shifts of the O $1s$, Ca $2p$, and Pr $3d$ core levels indicate that the change in the Madelung potential has negligible effects on the core-level shifts because it would cause shifts of the core levels of the O^{2-} anion and the Ca^{2+} and Pr^{3+} cations in different directions. Core-hole screening by conduction electrons can also be excluded from the

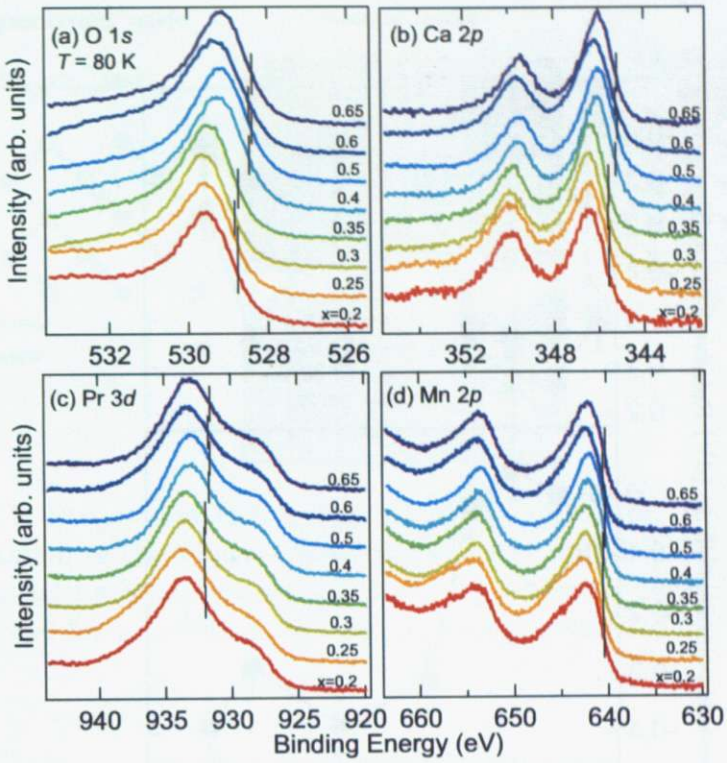

Figure 3.5: Core-level photoemission spectra of $Pr_{1-x}Ca_xMnO_3$ taken with the Mg $K\alpha$ line at 80 K. (a) O 1s; (b) Ca 2p; (c) Pr 3d; (d) Mn 2p. The intensity has been normalized to the peak height.

main origin of the core-level shifts in transition-metal oxides [3.10, 13]. The chemical-shift term is important for the Mn 2p core-level shift because of the increase in the Mn valence with hole doping from Mn^{3+} towards Mn^{4+}. Therefore, we consider that the shifts of the O 1s, Ca 2p, and Pr 3d core levels are largely due to the chemical potential shift $\Delta\mu$, and take the average of the shifts of the three core levels as a measure of $\Delta\mu$ in PCMO at 80 K.

In Fig. 3.6(b), we have plotted $\Delta\mu$ at 80 K in PCMO as a function of hole concentration. The shift was large in the CO region $x \lesssim 0.5$. This may be related with the fixed periodicity of the stripes in PCMO at low temperatures for $x < 0.5$ as shown in Fig. 3.6(c) [3.14]. On the other hand, the suppression of the $\Delta\mu$ was observed in the CO region $x \gtrsim 0.5$. If the suppression of the chemical potential shift is due to an electronic PS as the thermodynamic relationship suggests, in order to gain the long-range Coulomb energy the PS should occur only on a microscopic scale as

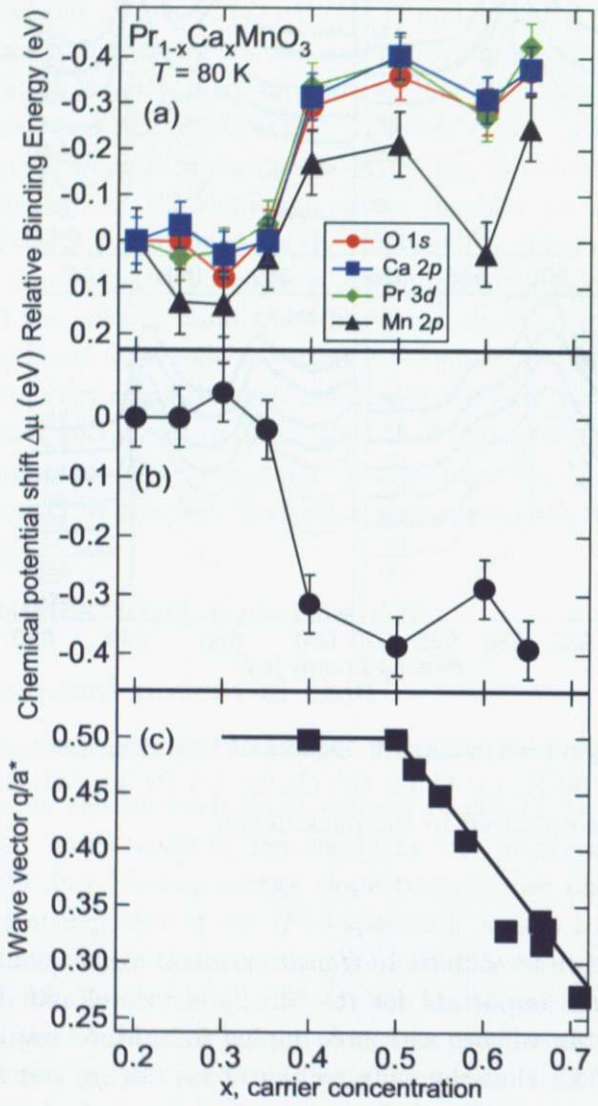

Figure 3.6: Core-level shifts, chemical potential shift and the wave vector of charge modulation at 80 K in $Pr_{1-x}Ca_xMnO_3$ [3.14]. (a) Binding energy shifts of the O 1*s*, Ca 2*p*, Pr 3*d*, and Mn 2*p* core levels as functions of carrier concentration x; (b) Chemical potential shift $\Delta\mu$ as a function of carrier concentration x; (c) Wave vector of the charge modulation versus carrier concentration for $Pr_{1-x}Ca_xMnO_3$ [3.14].

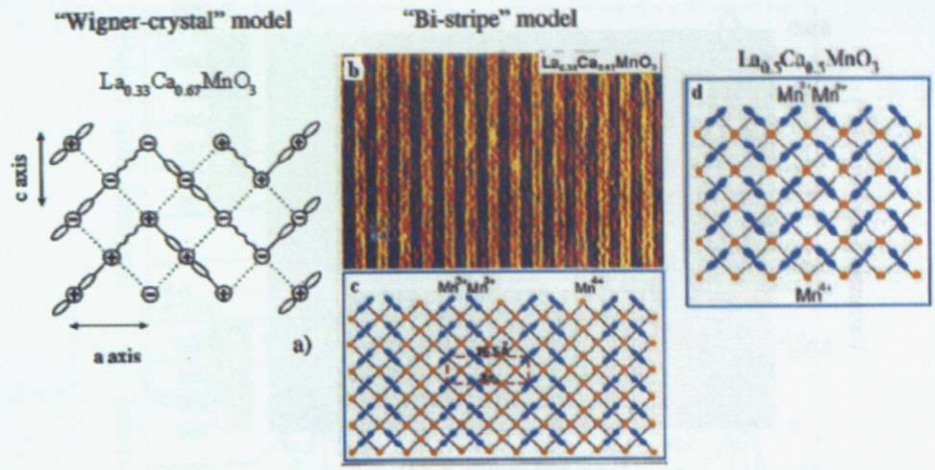

Figure 3.7: Stripe formation in $La_{1-x}Ca_xMnO_3$ [3.15, 16]. (a) Schematic representation of the Wigner-crystal model for $x = 0.67$ [3.16]. (b) High-resolution lattice image obtained at 95K; (c) Schematic picture of the bi-stripe model for $x = 0.67$ [3.15]. (d) Schematic picture of the stripes for $x = 0.5$.

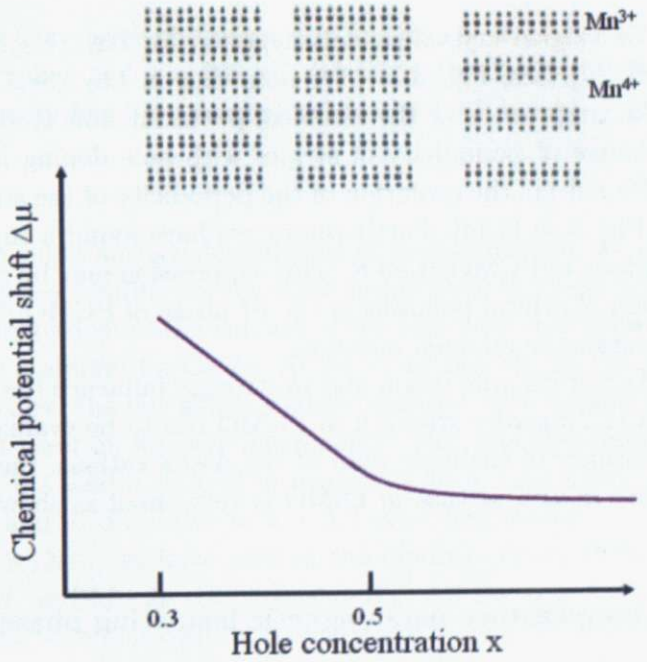

Figure 3.8: Schematic image of the chemical potential shift in the case of stripe formation in $Pr_{1-x}Ca_xMnO_3$ related to CE-type charge-ordered phase.

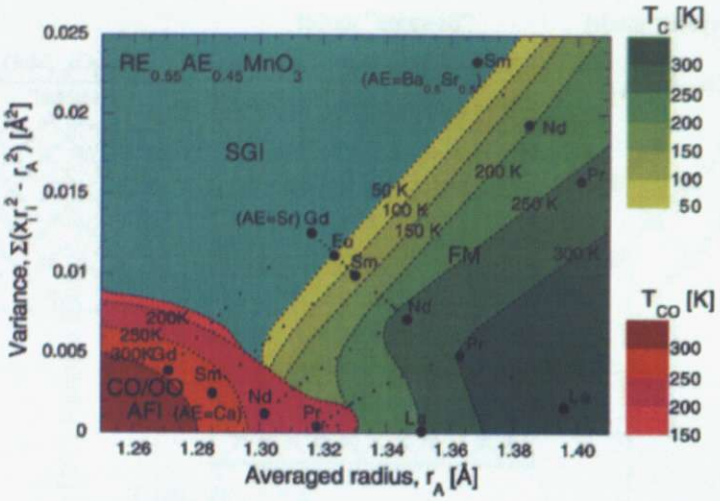

Figure 3.9: Electronic phase diagram of $RE_{1-x}AE_xMnO_3$ in the plane of the averaged A-site radius and the variance of the A-site ionic radius [3.20]. FM, CO/OO AFI, and SGI denote ferromagnetic metal, charge/orbital-ordered antiferromagnetic insulator, and spin glasslike insulator, respectively.

in the bi-stripe or Wigner-crystal model suggested for $La_{1-x}Ca_xMnO_3$ for $x \geq 0.5$ [3.15, 16, 17] (see, Fig. 3.7). We note that in $La_{2-x}Sr_xCuO_4$ and $La_{2-x}Sr_xNiO_4$ the suppression of the chemical potential shift is most likely related to the change of periodicity of stripes with hole doping [3.10, 18]. The $\Delta\mu$ in PCMO reflects the evolution of the periodicity of the stripes (see Fig. 3.6(c) and Fig. 3.8) [3.14]. Furthermore, we have found a suppression of the $\Delta\mu$ in FI phase of PCMO at 80 K. This suppression may be connected with the formation of orbital polarons in the FI phase of PCMO [3.19], but its mechanism remains as an open question.

Since the effect of disorder was found to strongly influence the chemical potential shift [3.11], disorder strength in PCMO has to be evaluated. According to the variance of the ionic radii of the A-site cations, the effect of disorder in PCMO as well as that in LSMO is very small as shown in Fig. 3.9 [3.20, 21].

3.3.1.2 High-temperature paramagnetic insulating phase

Figure 3.10 shows the photoemission spectra of the O 1*s*, Ca 2*p*, Pr 4*d*, and Mn 2*p* core levels taken at $h\nu = 800$ eV. The line shapes of most of the core levels did not change significantly for these compositions. Nevertheless, because the line shape on the higher binding energy side of the O 1*s* was

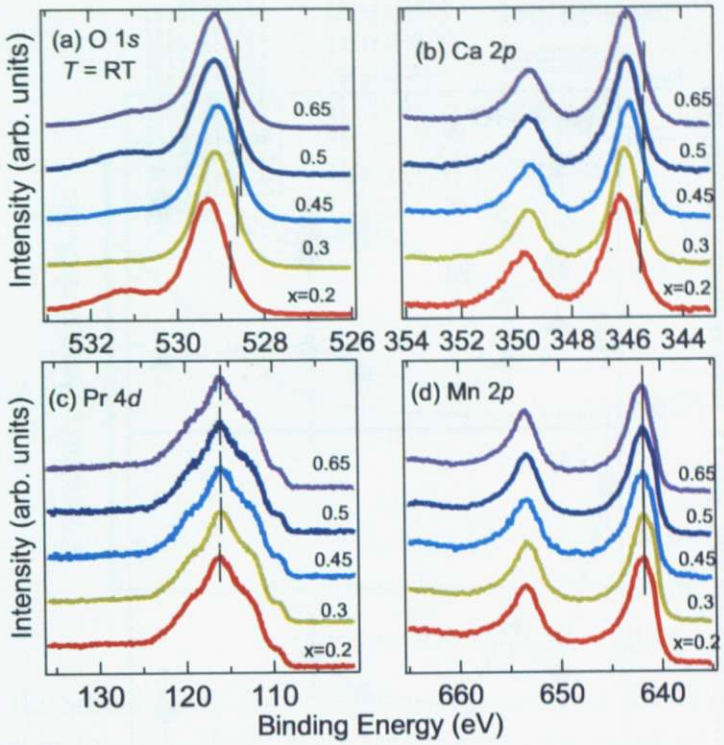

Figure 3.10: Core-level photoemission spectra of $Pr_{1-x}Ca_xMnO_3$ at room temperature taken at $h\nu = 800$ eV. (a) O 1s; (b) Ca 2p; (c) Pr 4d; (d) Mn 2p. The intensity has been normalized to the peak height.

sensitive to a slight surface degradation or contamination, we used the midpoint of the lower binding energy slope rather than the peak position for the O 1s core level to deduce the amount of the core-level shift more reliably. We also used the midpoint for Ca 2p. As for Pr 4d and Mn 2p, the peak position was used because the line shape slightly changed with doping and therefore the midpoint position was less meaningful. Also, the photoemission spectra for $x = 0.25$, 0.3, and 0.35 were measured at $h\nu = 1253.6$ eV, and the shifts of $x = 0.25$, and 0.35 relative to $x = 0.3$ were determined.

In Fig. 3.11(a), we have plotted the binding energy shifts of the O 1s, Ca 2p, Pr 4d, and Mn 2p core levels at RT. All the core levels have shown identical shifts with hole concentration except for the Mn 2p core level, where the effect of chemical shift is superimposed. Therefore, we assume that the shifts of the O 1s, Ca 2p, and Pr 4d core levels are largely due to the chemical potential shift, and take the average of the shifts of the three core levels as a measure of $\Delta\mu$ as a function of hole concentration at RT in PCMO.

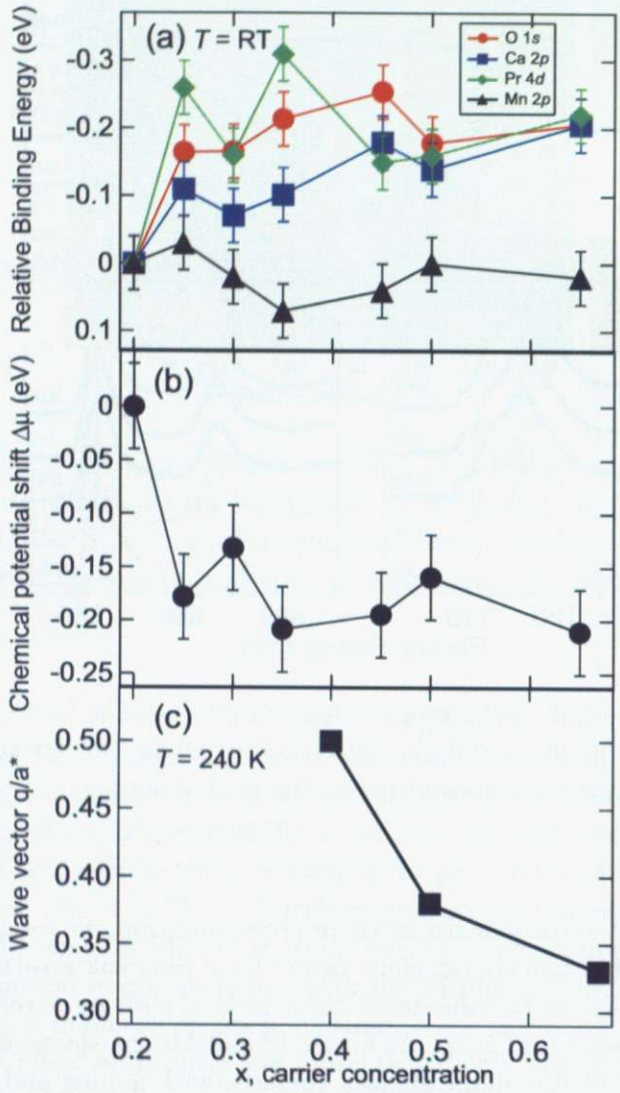

Figure 3.11: Core-level shifts and chemical potential shift at room temperature and wave vector of the charge modulation at 240 K in $Pr_{1-x}Ca_xMnO_3$ [3.14]. (a) Binding energy shifts of the O 1*s*, Ca 2*p*, Pr 4*d*, and Mn 2*p* core levels as functions of carrier concentration x; (b) Chemical potential shift $\Delta\mu$ as a function of carrier concentration x; (c) Wave vector of charge modulation versus carrier concentration for $Pr_{1-x}Ca_xMnO_3$ at 240 K [3.14].

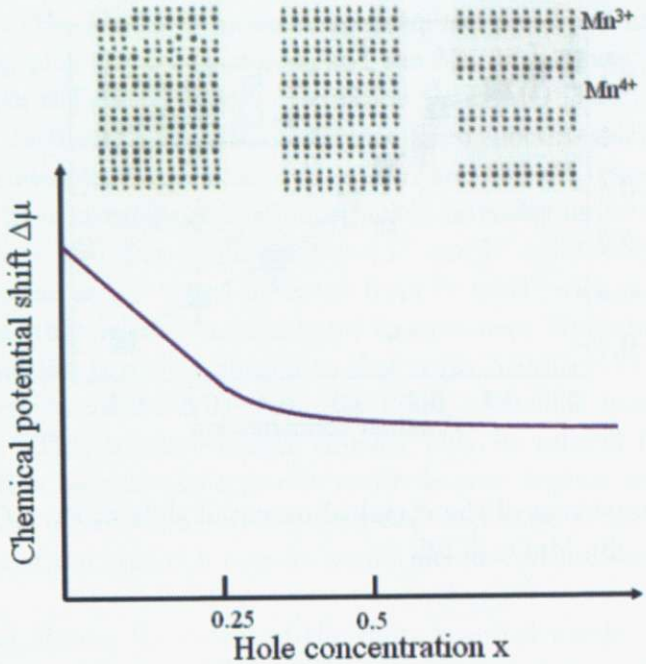

Figure 3.12: Schematic image of the chemical potential shift for the stripe fluctuation in $Pr_{1-x}Ca_xMnO_3$ in paramagnetic insulating phase.

In Fig. 3.11(b), we have plotted $\Delta\mu$ in PCMO thus deduced as a function of carrier concentration. The shift was large in the region $x \lesssim 0.25$, which may be understood in analogy to the case of LSMO [3.12]. The suppression of the chemical potential shift was observed near and in the CO region $x \gtrsim 0.3$. Although our measurements were done in the PI phase above the CO transition temperature, fluctuations of the CO state are expected to be present in the PI phase as was observed by means of x-ray resonant scattering [3.22]. In fact, the structural modulation wave vector in PCMO changes with carrier concentration at high temperatures in the CO composition range as shown in Fig. 3.11(c), which is related to the pinning of chemical potential (see Fig. 3.12) [3.14]. Also, from the observed suppression of $\Delta\mu$ in the region around $x \sim 0.3$, which exhibits the ferromagnetic insulating phase at low temperatures, we speculate that the fluctuation of the CO state also exist over a finite concentration range around the phase boundary at $x = 0.3$.

In Fig. 3.13, we compare $\Delta\mu$ for PCMO at RT with that for LSMO. For $x \lesssim 0.25$, both $\Delta\mu$ curves show similar doping dependences in the sense that the shifts are monotonous. The difference between the two become

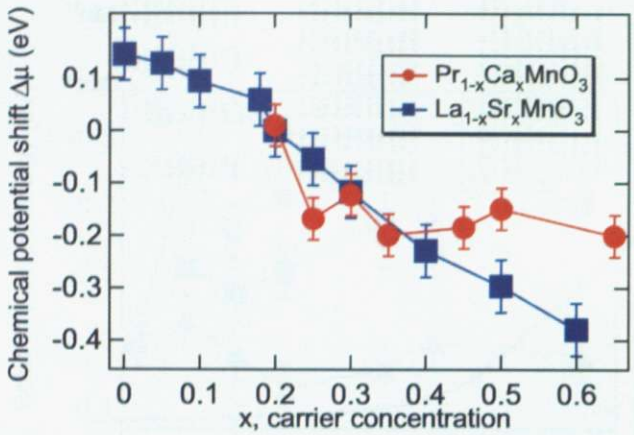

Figure 3.13: Comparison of the chemical potential shift in $Pr_{1-x}Ca_xMnO_3$ with that in $La_{1-x}Sr_xMnO_3$ [3.12].

pronounced for $x \gtrsim 0.3$, where the CO state occurs or the fluctuation of CO state becomes significant in PCMO but not in LSMO. Therefore, the different chemical potential shifts in PCMO and LSMO indeed reflect the CO in PCMO, and the μ pinning in the CO state of PCMO can be understood as due to the stronger tendencies toward "PS" in PCMO. Considering the suppression of $\Delta\mu$ in PCMO, the absence of such suppression in LSMO and the much stronger CMR in PCMO than in LSMO, it is possible that the tendency towards electronic "PS" on a microscopic scale is the origin of CMR in manganite with CO state.

3.3.2 Spectral-weight transfer near Fermi level (E_F)

Valence-band spectra of PCMO at RT taken at different photon energies are shown in Fig. 3.14(a). The spectra mainly consisted of structures as labeled A, (A',) B, C, (C', C",) and D. The spectra taken at $h\nu = 930$ and 643.6 eV correspond to Pr $3d$-$4f$ and Mn $2p$-$3d$ on-resonance PES spactra, respectively. From the Mn $2p$-$3d$ resonance spectra, Mn $3d$-derived features appeared as structures A', C', and D. Structures A' and C' are shifted slightly toward higher binding energies than A and C, respectively, due to the different matrix elements between normal PES and resonant PES. Also, the intensity of structure C" was strongly enhanced in the Pr $3d$-$4f$ resonance spectra. The UPS ($h\nu = 21.2$ eV) spectrum represents the O $2p$ state due to the large relative photo-ionization cross-section of O $2p$ at low photon energies. Therefore, structures A, B, C, and D in the UPS spectrum

are assigned to the Mn $3d$-O $2p$ bonding state, the non-bonding O $2p$ state, the Mn $3d$ t_{2g} plus the Pr $4f$ states, and the Mn $3d$ e_g state, respectively, consistent with the cluster-model calculation for LSMO [3.23].

Figure 3.14(b), 3.14(c) show the valence-band spectra near E_F at RT for various hole concentrations taken at $h\nu = 21.2$ and 600 eV, respectively. The spectra have been normalized to the integrated intensity in the energy range from 1.5 eV to $\sim E_F$. Two features labeled D' and D" were observed in these spectra. Spectral weight was transferred from D' to D" with increasing hole concentration, that is, the valence-band spectra near E_F exhibited highly non-rigid-band-like behavior, similar to that in the LSMO [3.23, 24]. Similar behaviors have been widely observed in filling-controlled transition-metal oxides [3.25]. This spectral-weight transfer may be related to dynamical stripe formation because the hole-rich and hole-poor regions would give rise to the low and high binding energy features, respectively, and the relative contributions of the hole-rich regions would increase with hole doping [3.26, 27].

Next, we discuss the origin of the finite spectral weight at E_F in the insulating phase of PCMO. The spectra in a narrow energy region near E_F are shown in the inset of Fig. 3.14(b). For $x = 0.2$, and 0.25, the insulating gap was opened. For $x \gtrsim 0.3$, a finite intensity at E_F was observed in the PI phase, leading to the pseudogap behavior. Recently, a finite intensity at E_F was observed in the photoemission spectra of $Nd_{1-x}Sr_xMnO_3$ in the PI phase above the Curie temperature of the FM metallic phase [3.28]. Kajimoto *et al.* [3.29] have remarked that FM fluctuations exist in the PI phase of the PCMO by means of neutron scattering studies. Theoretically, FM fluctuations in the CO state of PCMO was found to lead to metallic character using a combination of numerical relaxation technique and analytic mean-field approximation [3.30]. On the other hand, from the x-ray resonant scattering studies, the CO fluctuations were also observed in the PI phase of the PCMO [3.22]. Therefore, we consider that the pseudogap features for $x \gtrsim 0.3$, namely, the density of states (DOS) minimum and the finite intensity at E_F are caused by the CO fluctuations and FM fluctuations, respectively as indicated in Fig. 3.15. Monte Carlo simulations on the PS model have shown that the pseudogap behavior is caused by the formation of FM metallic clusters in an insulating background, and the resultant mixed-phase state is crucial for the pseudogap formation [3.31, 32]. In the PI phase of $Bi_{1-x}Ca_xMnO_3$, an atomic-scale image of PS into FM metallic and insulating regions was observed by means of scanning tunneling microscopy, and it is considered that the FM fluctuations are related to thermally activated hopping of e_g electrons induced by DE mechanism at high temperatures [3.33, 34, 35]. Recently, by angle-resolved photoemission

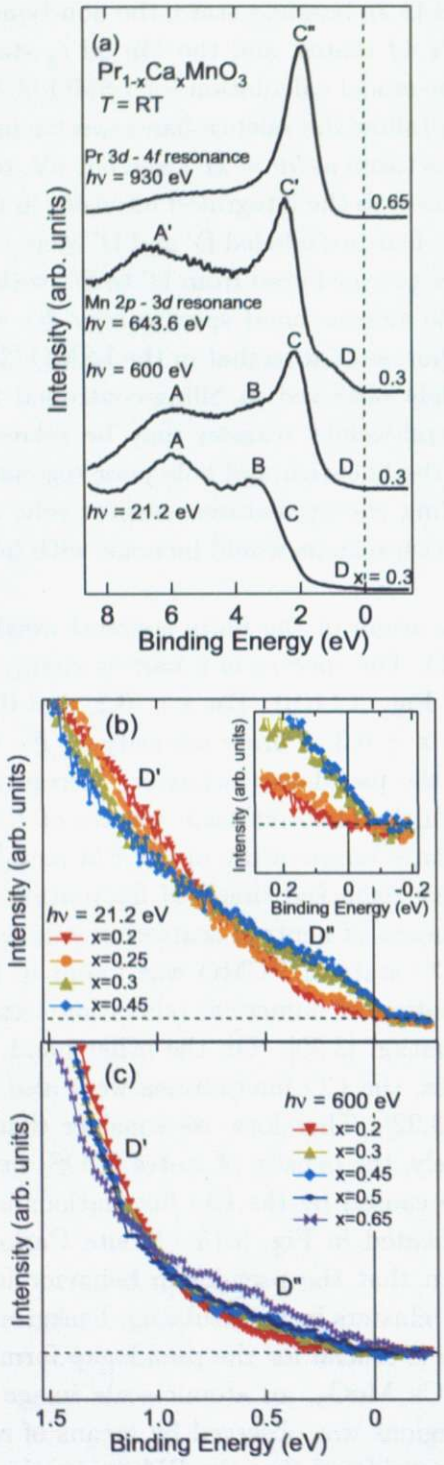

Figure 3.14: Valence-band photoemission spectra of $Pr_{1-x}Ca_xMnO_3$ at room temperature. (a) Comparison of spectra taken at various photon energies; (b) Spectra near E_F taken at $h\nu = 21.2$ eV; (c) $h\nu = 600$ eV.

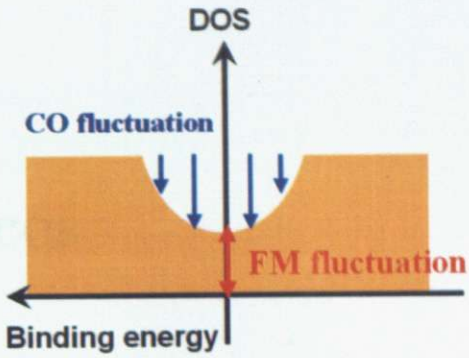

Figure 3.15: Schematic image of pseudogap in $Pr_{1-x}Ca_xMnO_3$ induced by the competition between the FM and CO phases.

measurements, a pseudogap was observed in the low-temperature FM state of the bilayer compound $La_{1.2}Sr_{1.8}Mn_2O_7$ [3.36, 37]. The observations of the pseudogap behavior in manganites may provide an important clue for understanding the origin of the CMR effect.

3.4 Conclusion

We have experimentally determined the chemical potential shift $\Delta\mu$ as a function of carrier concentration in PCMO by means of core-level photoemission spectroscopy. The chemical potential shift was suppressed for $x \gtrsim 0.5$ at 80 K and around and in the CO composition range at RT, which we attribute to the change of periodicity of stripes in PCMO. Comparison with the chemical potential shift in LSMO implies that the electronic "PS" may be related to the origin of CMR in manganites with CO state. In the valence band near E_F of PCMO, spectral weight was transferred with hole doping, and for the CO region $x \gtrsim 0.3$ we observed the pseudogap behavior with a finite DOS at E_F, consistent with the presence of both FM and CO fluctuations in the PI phase.

References

[3.1] M. v. Zimmermann, C. S. Nelson, J. P. Hill, D. Gibbs, M. Blume, D. Casa, B. Keimer, Y. Murakami, C.-C. Kao, C. Venkataraman, T. Gog, Y. Tomioka, and Y. Tokura, Phys. Rev. B **64**, 195133 (2001).

[3.2] Y. Tomioka, A. Asamitsu, H. Kuwahara, Y. Moritomo, and Y. Tokura, Phys. Rev. B **53**, R1689 (1996).

[3.3] Z. Jirak, S. Krupica, Z. Simsa, M. Dlouha, and S. Vratislav, J. Magn. Magn. Mater **53**, 153 (1985).

[3.4] A. J. Millis, P. B. Littlewood, and B. I. Shraiman, Phys. Rev. Lett. **74**, 5144 (1995).

[3.5] S. Yunoki, J. Hu, A. L. Malvezzi, A. Moreo, N. Furukawa, and E. Dagotto, Phys. Rev. Lett. **80**, 845 (1998).

[3.6] A. Moreo, S. Yunoki, and E. Dagotto, Science **283**, 2034 (1999).

[3.7] S. Mori, C. H. Chen, and S.-W. Cheong, Phys. Rev. Lett. **81**, 3972 (1998).

[3.8] M. Uehara, S. Mori, C. H. Chen, and S.-W. Cheong, Nature **399**, 560 (1999).

[3.9] D. D. Sarma, Dinesh Topwal, U. Manju, S. R. Krishnakumar, M. Bertolo, S. La Rosa, G. Cautero, T. Y. Koo, P. A. Sharma, S.-W. Cheong, and A. Fujimori, Phys. Rev. Lett. **93**, 097202 (2004).

[3.10] A. Ino, T. Mizokawa, A. Fujimori, K. Tamasaku, H. Eisaki, S. Uchida, T. Kimura, T. Sasagawa, and K. Kishio, Phys. Rev. Lett. **79**, 2101 (1997).

[3.11] A. Moreo, M. Mayr, A. Feiguin, S. Yunoki, and E. Dagotto, Phys. Rev. Lett. **84**, 5568 (2000).

[3.12] J. Matsuno, A. Fujimori, Y. Takeda, and M. Takano, Europhys. Lett. **59**, 252 (2002).

[3.13] N. Harima, J. Matsuno, A. Fujimori, Y. Onose, Y. Taguchi, and Y. Tokura, Phys. Rev. B **64**, 220507(R) (2001).

[3.14] G. C. Milward, M. J. Calderon, and P. B. Littlewood, Nature **433**, 607 (2005).

[3.15] S. Mori, C. H. Chen, and S.-W. Cheong, Nature **392**, 473 (1998).

[3.16] P. G. Radaelli, D. E. Cox, L. Capogna, S.-W. Cheong, and M. Marezio, Phys. Rev. B **59**, 14440 (1999).

[3.17] While M. Tokunaga, Y. Tokunaga, M. Yasugaki, and T. Tamegai [J. Magn. Magn. Mater **226-230**, 851 (2001)] observed a macroscopic PS with length scale exceeding one micrometer in PCMO at $x = 0.3$ by means of magneto-optical measurements, the electronic "PS" such as stripes will be driven on a microscopic scale.

[3.18] M. Satake, K. Kobayashi, T. Mizokawa, A. Fujimori, T. Tanabe, T. Katsufuji, and Y. Tokura, Phys. Rev. B **61**, 15515 (2000).

[3.19] T. Mizokawa, D. I. Khomskii and G. A. Sawazky, Phys. Rev. B **63**, 024403 (2000).

[3.20] Y. Tomioka and Y. Tokura, Phys. Rev. B **70**, 014432 (2004).

[3.21] The Coulombic disorder due to the difference in the valence of the A-site cations may occur, but this effect is considered to be common in the filling controlled manganites. The pinning of the chemical potential shift in PCMO suggests that this disorder effect is also unimportant.

[3.22] M. v. Zimmermann, J. P. Hill, D. Gibbs, M. Blume, D. Casa, B. Keimer, Y. Murakami, Y. Tomioka, and Y. Tokura, Phys. Rev. Lett. **83**, 4872 (1999).

[3.23] T. Saitoh, A. E. Bocquet, T. Mizokawa, H. Namatame, A. Fujimori, M. Abbate, Y. Takeda, and M. Takano, Phys. Rev. B **51**, 13942 (1995).

[3.24] K. Horiba, A. Chikamatsu, H. Kumigashira, M. Oshima, N. Nakagawa, M. Lippmaa, K. Ono, M. Kawasaki, and H. Koinuma, Phys. Rev. B **71**, 155420 (2005).

[3.25] K. Maiti and D. D. Sarma, Phys. Rev. B **61**, 2525 (2000).

[3.26] A. Ino, C. Kim, M. Nakamura, T. Yoshida, T. Mizokawa, Z.-X. Shen, A. Fujimori, T. Kakeshita, H. Eisaki, and S. Uchida, Phys. Rev. B **62**, 4137 (2000).

[3.27] T. Yoshida, X. J. Zhou, T. Sasagawa, W. L. Yang, P. V. Bogdanov, A. Lanzara, Z. Hussain, T. Mizokawa, A. Fujimori, H. Eisaki, Z.-X. Shen, T. Kakeshita, and S. Uchida, Phys. Rev. Lett. **91**, 027001 (2003).

[3.28] A. Sekiyama, H. Fujiwara, A. Higashiya, S. Imada, H. Kuwahara, Y. Tokura, and S. Suga, cond-mat 0401601 (2004).

[3.29] R. Kajimoto, T. Kakeshita, Y. Oohara, H. Yoshizawa, Y. Tomioka, and Y. Tokura, Phys. Rev. B **58**, R11837 (1998).

[3.30] T. Hotta and E. Dagotto, Phys. Rev. B **61**, R11879 (2000).

[3.31] A. Moreo, S. Yunoki, and E. Dagotto, Phys. Rev. Lett. **83**, 2773 (1999).

[3.32] H. Aliaga, D. Magnoux, A. Moreo, D. Poilblanc, S. Yunoki, and E. Dagotto, Phys. Rev. B **68**, 104405 (2003).

[3.33] C. Renner, G. Aeppli, B.-G. Kim, Y.-A. Soh, and S.-W. Cheong, Nature **416**, 518 (2002).

[3.34] W. Bao, J. D. Axe, C. H. Chen, and S.-W. Cheong, Phys. Rev. Lett. **78**, 543 (1997).

[3.35] H. L. Liu, S. L. Cooper, and S.-W. Cheong, Phys. Rev. Lett. **81**, 4684 (1998).

[3.36] D. S. Dessau, T. Saitoh, C.-H. Park, Z.-X. Shen, P. Villella, N. Hamada, Y. Moritomo, and Y. Tokura, Phys. Rev. Lett. **81**, 192 (1998).

[3.37] Y.-D. Chuang, A. D. Gromko, D. S. Dessau, T. Kimura, and Y. Tokura, Science **292**, 1509 (2001).

Chapter 4

Temperature dependence of chemical potential and spectral-weight transfer in $Pr_{1-x}Ca_xMnO_3$

Part of this chapter has been published in

- "Temperature-dependent photoemission spectra, spectral-weight transfer, and chemical potential shift in $Pr_{1-x}Ca_xMnO_3$: Implications for charge density modulation" by K. Ebata, M. Hashimoto, K. Tanaka, A. Fujimori, Y. Tomioka, and Y. Tokura, Phys. Rev. B, **76**, 174418 (2007).
- "Photoemission Study of Perovskite-type Manganites with Stripe Ordering" by K. Ebata, H. Wadati, M. Takizawa, K. Maekawa, A. Fujimori, A. Chikamatsu, H. Kumigashira, M. Oshima, Y. Tomioka, H. Kuwahara, and Y. Tokura, J. Supercond. Nov. Magn. **20**, 543-546 (2007).

4.1 Introduction

Many experimental and theoretical studies have indicated that the inhomogeneous nature arising from competition between the ferromagnetic (FM) metallic and antiferromagnetic (AF) insulating states leads to a large change in the resistivity as a function of temperature, magnetic field, chemical pressure and so on. A presence of coexsisting clusters of FM charge-disordered and AF charge-ordered (CO) states in $(La_{1-y}Pr_y)_{1-x}Ca_xMnO_3$ was clearly shown by means of electron microscopy [4.1]. Fluctuations between the

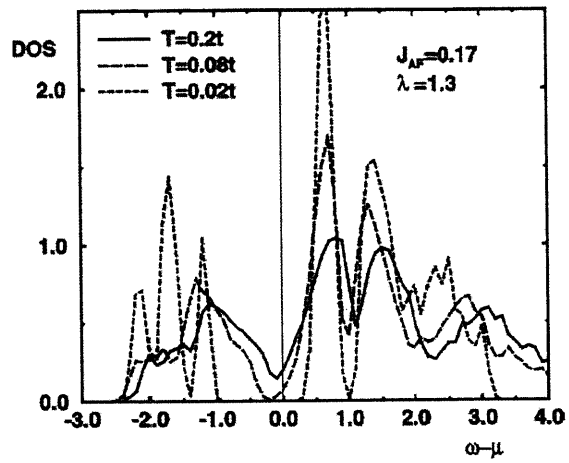

Figure 4.1: Temperature-dependent density of states obtained from the double-exchange model with Jahn-Teller distortion in manganites. T, J_{AF} and λ denote temperature, antiferromagnetic coupling between nearest-neighbor t_{2g} spins and dimensionless coupling constant, respectively [4.5].

FM and CO phases were found in the paramagnetic insulating (PI) phase of $Pr_{1-x}Ca_xMnO_3$ (PCMO) by means of neutron scattering and x-ray resonant scattering studies [4.2, 3]. From the studies of photoemission spectroscopy (PES), pseudogap features with a finite intensity at the Fermi level (E_F) were observed in the PI phase of PCMO, consistent with the fluctuations involving both phases as indicated in Chapter 3 [4.4]. Monte Carlo simulations on a two-orbital model showed a temperature evolution of the density of states (DOS) from a clear gap due to the charge ordering at low temperatures to a pseudogap in the competing phases at high temperatures as shown in Fig. 4.1 [4.5]. The calculation also demonstrated the gaps in the CO phase of the manganites were much larger than k_BT_{CO} (T_{CO} : CO transition temperature) [4.6]. Okimoto *et al.* [4.7] showed the existence of an optical gap in the CO phase of PCMO. From valence-band PES and O K edge x-ray absorption studies, Dalai *et al.* [4.8] revealed that the charge-transfer energy of PCMO takes a large value, consistent with the strong charge localization in PCMO. Furthermore, the gap in the CO phase was detected in $Nd_{1-x}Sr_xMnO_3$ (NSMO) by means of PES and tunneling spectroscopy as shown in Fig. 4.2 [4.9, 10]. Small bandwidth systems such as PCMO exhibit a so-called CE-type AF CO state and the CMR effect becomes large owing to the collapse of the CO state under a magnetic field [4.11]. PCMO has a particularly stable CO state over a wide hole concen-

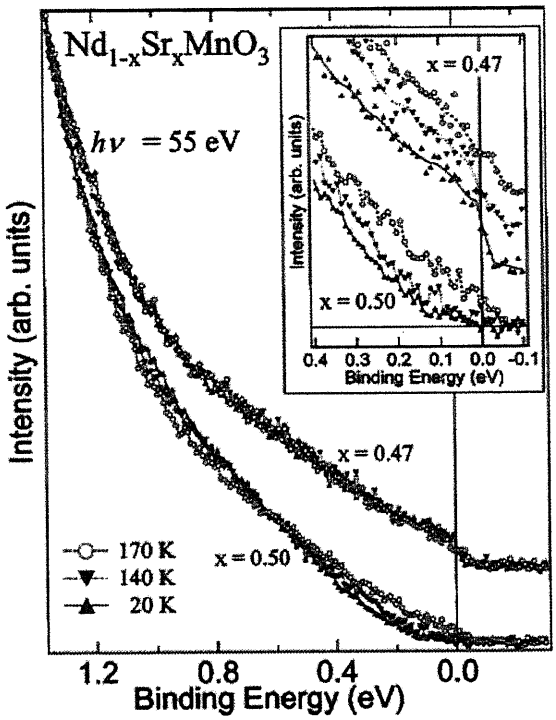

Figure 4.2: Photoemission spectra near E_F in $Nd_{1-x}Sr_xMnO_3$ ($x = 0.47$ and 0.5) taken at 20, 140, and 170 K [4.9].

tration range as shown in Fig. 4.3 [4.11, 12, 13]. In addition, PCMO shows an insulator-to-metal transition under various external perturbations such as electric field [4.14], high pressure [4.15], and light irradiation [4.16, 17].

In this chapter, we report on the results of a detailed temperature-dependent PES study of PCMO, which shows CMR for $x \geq 0.3$. PCMO is suitable for clarifying the relationship between the temperature-dependent DOS determined by PES and the two-orbital model because the PCMO is considered to show the CO gap at low temperatures and the pseudogap at high temperatures [4.4, 7, 5]. We observed a pseudogap with a finite DOS at E_F in the high-temperature PI phase and a clear gap opening in the low-temperature CO phase, indicating competition between the FM and CO phases. Also, the spectra in the CO phase showed a remarkable temperature dependence. For $x < 0.3$, on the other hand, the DOS at E_F was found to be low in the PI phase and the spectra in the ferromagnetic insulating (FI) phase showed no significant temperature dependence. The gap was opened in the FI and CO phases and an upward chemical potential shift ($\Delta\mu$) with

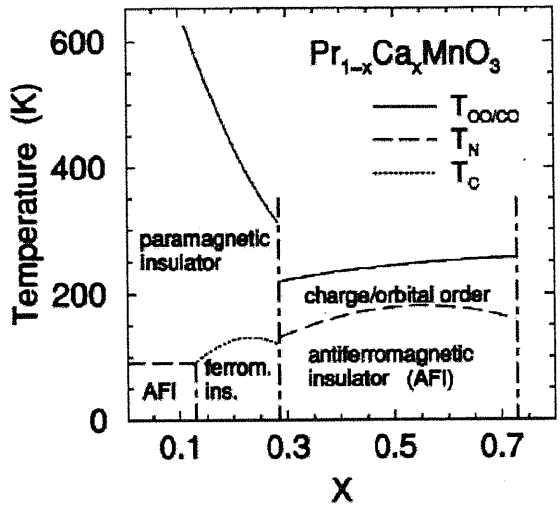

Figure 4.3: Electronic phase diagram of $Pr_{1-x}Ca_xMnO_3$ [4.11, 12, 13].

decreasing temperature was observed. When the charge modulation wave vector as a function of hole concentration in the CO phase of PCMO became constant at low temperatures, the doping dependent chemical potential shift became large and monotonic, probably related to the spectral weight transfer near the E_F with hole doping.

4.2 Experimental

Single crystals of PCMO with the Ca concentrations of x = 0.2, 0.25, 0.3, 0.35, 0.4, 0.5, 0.6, and 0.65 were grown by the floating-zone method. These samples were supplied by Dr. Y. Tomioka and Prof. Y. Tokura of National Institute of Advanced Industrial Science and Technology. The growth techniques and transport properties of the crystals were described in Ref.[4.11]. Ultraviolet photoemission spectroscopy (UPS) and x-ray photoemission spectroscopy (XPS) measurements were performed using the photon energy of $h\nu = 21.2$ eV (He I) and $h\nu = 1253.6$ eV (Mg $K\alpha$). All the photoemission measurements were performed under the base pressure of $\sim 10^{-10}$ Torr at 80-300 K. The samples were repeatedly scraped *in situ* at several temperatures with a diamond file to obtain clean surfaces. In the case of UPS, the scraping was made until a bump around 9-10 eV, which was attributed to surface contamination, decreased and the valence-band spectra did not change with further scraping. In the case of XPS, the cleanliness of the sample surface was checked by the reduction of the shoulder on the high

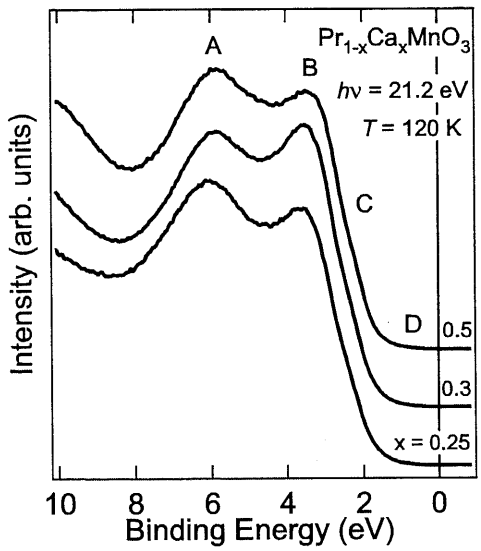

Figure 4.4: Valence-band photoemission spectra of $Pr_{1-x}Ca_xMnO_3$.

binding energy side of the O 1*s* core level. Photoelectrons were collected using a Scienta SES-100 electron-energy analyzer. The energy resolution was about 15 meV for He I and 800 meV for Mg $K\alpha$.

4.3 Results and discussion

4.3.1 Valence-band spectra

Figure 4.4 shows PES spectra in the valence-band region of PCMO at 120 K. The spectra consisted of four main structures labeled A, B, C, and D, which are assigned to the Mn 3*d*-O 2*p* bonding state, the non-bonding O 2*p* state, the Mn 3*d* t_{2g} plus the Pr 4*f* states, and the Mn 3*d* e_g state, respectively [4.4].

Figure 4.5(a)-(c) show the temperature-dependent spectra near E_F for the three compositions. The spectra have been scaled in order to normalize the integrated intensity in the energy range from binding energy $E_B = 1.2$ eV to above E_F. For $x = 0.3$ and 0.5, below T_{CO} we observed the opening of a gap due to the CO phase. We have estimated the magnitude of the gaps by linearly extrapolating the spectra to the abscissa, as shown by dotted lines in Fig. 4.5. The magnitude of the CO gap was estimated to be about 250 meV for $x = 0.3$ and 150 meV for $x = 0.5$ at 80 K, consistent with

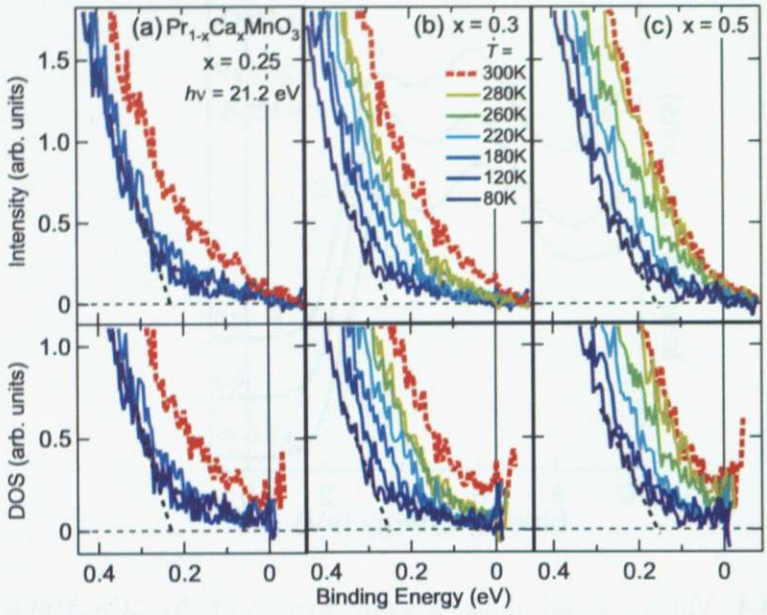

Figure 4.5: Temperature-dependent photoemission spectra near E_F of $Pr_{1-x}Ca_xMnO_3$, (a) $x = 0.25$; (b) $x = 0.3$; (c) $x = 0.5$. The bottom panels show the density of states (DOS) obtained by dividing the spectrum in the upper panels by the Fermi Dirac function. Dotted lines indicate the estimate of the gap (see text).

the optical gap energy estimated to be about 180 meV at 10 K for PCMO with $x = 0.4$ [4.7]. By PES measurements, Sekiyama *et al.* [4.9] found a CO gap in NSMO ($x = 0.5$), too, and estimated the magnitude to be about 100 meV. The magnitude of the CO gaps in manganites is much larger than k_BT_{CO}, in agreement with the prediction of the Monte Carlo simulation on the two-orbital model [4.6]. On the other hand, for $x = 0.25$, there was a gap structure at all temperatures and the FI gap was estimated to be about 230 meV [4.18].

We shall discuss the temperature dependence of the spectra near E_F of PCMO within the CO and FI phases in more detail. There was a significant temperature variation within the CO phase for $x = 0.3$ and 0.5 while little temperature dependence was observed within the FI phase for $x = 0.25$. From an x-ray resonant scattering study, Zimmermann *et al.* [4.12] found that for PCMO with $x = 0.4$ and 0.5 while long-range charge order was present, short-range orbital order was also realized. On the other hand, for PCMO with $x = 0.25$, long-range orbital order was observed with no

indication of charge ordering [4.12]. As a result, the correlation lengths of orbital order had temperature dependence for $x = 0.4$ and 0.5 but not for $x = 0.25$ [4.12]. Therefore, the difference in the temperature evolution of the gap structures between the FI and CO phases may be related to the different temperature dependence of the correlation lengths of orbital order in both phases. Recently, the CO gap in NSMO ($x = 0.5$) was also found to show temperature dependence by means of PES and tunneling spectroscopy [4.9, 10].

In order to eliminate the effect of the temperature dependence of the Fermi Dirac function and to extract the intrinsic temperature-dependent changes of the DOS, we have divided each PES spectrum by the Fermi Dirac function at each temperature as shown in the bottom panels of Fig. 4.5. While the insulating gaps were opened at all temperatures for $x = 0.25$, finite intensity at E_F was observed in the PI phase of $x = 0.3$ and 0.5 [4.4]. The presence of the pseudogap, i.e., a gap-like feature with a finite DOS at E_F, at high temperatures and the real gap opening in the CO phase for $x = 0.3$ and 0.5 are in good qualitative agreement with Monte Carlo calculation with competition between the CO and FM phases [4.5]. It was also shown by the neutron scattering and x-ray resonant scattering experiments that both FM and CO fluctuations were present above T_{CO} in PCMO [4.2, 3]. We therefore consider that the pseudogaps appear when the insulating and metallic phases are competing with each other.

In Fig. 4.6, we have plotted the spectral weight obtained by integrating the spectra from $E_B = -0.05$ eV to 0.3 eV and from $E_B = -0.05$ eV to 0.1 eV in PCMO as functions of temperature. The gradual increase of spectral weight near E_F with temperature rather than a sudden jump at T_{CO} is probably related with the thermally activated hopping of e_g electrons at high temperatures as reported for $Bi_{1-x}Ca_xMnO_3$ [4.19, 20]. In the previous PES studies of the FM phase of $La_{1-x}Sr_xMnO_3$ (LSMO) ($x = 0.4$), the decreasing spectral weight at E_F with increasing temperature was observed and was attributed to spectral weight transfer from the coherent to the incoherent parts with increasing temperature [4.21, 22]. The temperature-dependent change of the spectral weight at E_F in PCMO which exhibits CO phase was opposite to that in LSMO ($x = 0.4$). The different temperature evolution of the DOS for the different types of ground states may be related to the two different types of CMR: (1) CMR which occurs in the high temperatures paramaganetic regime as in the case of LSMO, where the system undergoes a PI to FM transition upon cooling; (2) CMR which occurs in the CO phase at low temperature due to the melting of the CO state under magnetic field as in the case of PCMO.

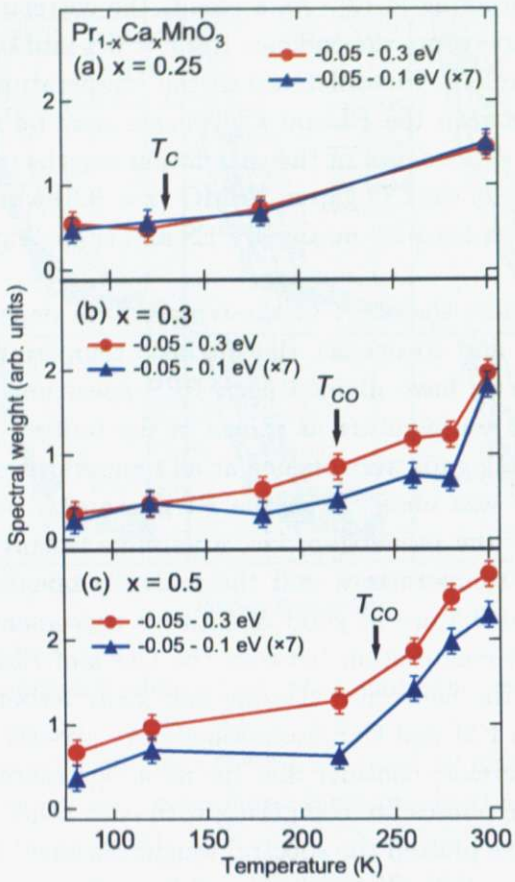

Figure 4.6: Spectral weight integrated from $E_B = -0.05$ eV to 0.3 eV and that from $E_B = -0.05$ eV to 0.1 eV in $Pr_{1-x}Ca_xMnO_3$ as functions of temperature, (a) $x = 0.25$; (b) $x = 0.3$; (c) $x = 0.5$. T_C and T_{CO} denote the Curie temperature and the charge ordering temperature, respectively. All the spectra have been scaled in order to normalize the integrated intensity in the wide energy range of $E_B = 1.2$ eV to $\sim$ above E_F.

4.3.2 Chemical potential shift

Next, we deduce the composition and temperature dependent chemical potential shift and discuss its implications of the charge modulations and fluctuations in PCMO. In order to deduce the amount of the chemical potential shift, we have used the peak position of the Mn 3*d*-O 2*p* bonding state because the peak position of the non-bonding O 2*p* state was affected by the Pr 4*f* state whose intensity changes with x. In Fig. 4.7, we have plotted the

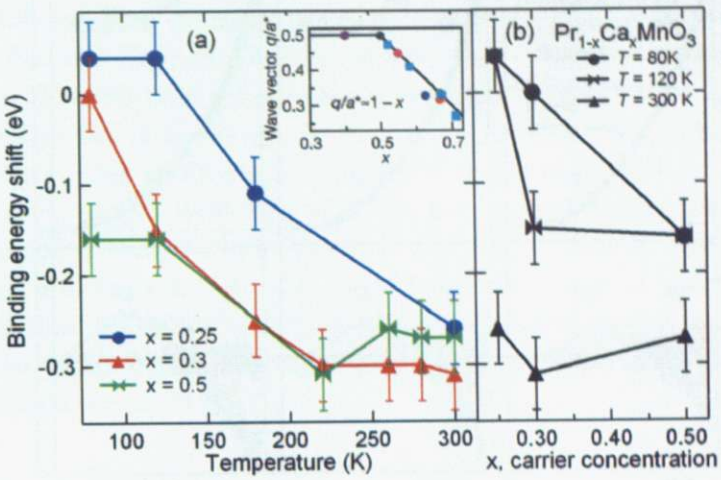

Figure 4.7: Binding energy shift as a function of temperature (a) and carrier concentration (b) in $Pr_{1-x}Ca_xMnO_3$. Inset shows the wave vector of the modulation versus carrier concentration x for $Pr_{1-x}Ca_xMnO_3$ and $La_{1-x}Ca_xMnO_3$ at low temperatures [4.23].

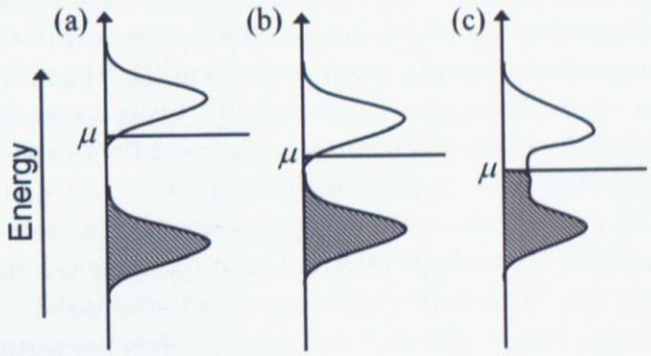

Figure 4.8: Schematic pictures of the temperature-dependent DOS and chemical potential shift in the charge-ordered (CO) composition range of $Pr_{1-x}Ca_xMnO_3$. (a) Low-temperature CO phase; (b) intermediate-temperature CO phase; (c) high-temperature paramagnetic insulating (PI) phase. μ denotes chemical potential.

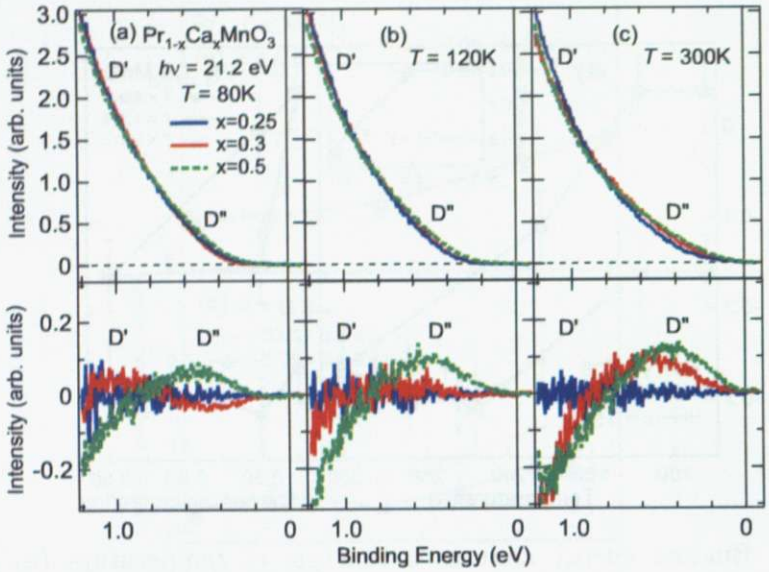

Figure 4.9: Hole-concentration dependent photoemission spectra near E_F of $Pr_{1-x}Ca_xMnO_3$, (a) $T = 80$ K; (b) $T = 120$ K; (c) $T = 300$ K. The bottom panels show the difference spectra obtained by subtracting the spectra of $x = 0.25$.

shift as a function of temperature and carrier concentration in PCMO. Panel (a) shows that an upward chemical potential shift occurred with decreasing temperature. We attribute it to the opening of gap in the FI and CO phases of PCMO. In Fig. 4.8, a schematic diagram for the temperature-dependent chemical potential shift in the CO composition range of PCMO is shown. In the CO phase, the CO gap is opened corresponding to the charge ordering in the CE-type AF state. If the hole concentration is less than $x = 0.5$, the upper band is partially occupied by electrons, and the chemical potential is located near its bottom. Therefore, the chemical potential is shifted upward with decreasing temperature. For $x \gtrsim 0.3$, we also observed a suppression of the chemical potential shift at high temperatures and a smooth shift at low temperatures with carrier concentration as shown in Fig. 4.7(b). We consider that the shifts is related to the evolution of the periodicity of stripes in PCMO as inferred from the chemical potential shift determined from the core-level photoemission spectra as described in Chapter 3 [4.4].

4.3.3 Spectral-weight transfer near Fermi level (E_F)

In Fig. 4.9, we have plotted the valence-band spectra of the three samples near E_F as a function of hole concentration. Spectral weight transfer from D' to D" with hole concentration was clearly observed at $T = 300$ K as repeated in Ref.[4.4], as can be seen from the difference spectra in the bottom panel. This effect can be attributed to the change of periodicity in the fluctuating stripes with hole concentration at high temperatures [4.23]. With decreasing temperature, the spectral weight transfer was gradually suppressed, concomitant with the recovery of the chemical potential shift. It is likely that the different behavior of the spectral weight transfer with hole concentration reflects the different evolution of the periodicity of the charge modulation in PCMO.

4.4 Conclusion

We have studied the temperature dependence of the DOS around E_F in PCMO by means of PES and observed a clear gap opening in the CO phase and a pseudogap with a finite intensity at E_F in the high-temperature PI phase for $x = 0.3$ and 0.5. The spectra within the CO phase also showed significant temperature dependence, probably related to the temperature dependence of the short-range orbital ordering. The temperature-dependent redistribution of spectral weight for $x = 0.3$ and 0.5 below and above T_{CO} was in good qualitative agreement with the results of the Monte Carlo simulation on a model for manganite with competing CO and FM fluctuations. For $x = 0.25$, a clear gap feature was found at all temperatures and the spectra within the FI phase showed little temperature dependence, which may be connected with the stable long-range orbital ordering. The temperature-dependent chemical potential shift was also observed in PCMO. We consider the shift to be related with the opening of the gap in the FI and CO phases. The hole-concentration dependent chemical potential shift was found to be suppressed at high temperatures, which we attribute to the charge self-organization such as stripes. Also, the spectral weight transfer with hole concentration was weakened with decreasing temperature, probably related to the recovery of the hole-concentration dependent chemical potential shift in PCMO at low temperatures.

References

[4.1] M. Uehara, S. Mori, C. H. Chen, and S.-W. Cheong, Nature **399**, 560 (1999).

[4.2] R. Kajimoto, T. Kakeshita, Y. Oohara, H. Yoshizawa, Y. Tomioka, and Y. Tokura, Phys. Rev. B **58**, R11837 (1998).

[4.3] M. v. Zimmermann, J. P. Hill, D. Gibbs, M. Blume, D. Casa, B. Keimer, Y. Murakami, Y. Tomioka, and Y. Tokura, Phys. Rev. Lett. **83**, 4872 (1999).

[4.4] K. Ebata, H. Wadati, M. Takizawa, A. Fujimori, A. Chikamatsu, H. Kumigashira, M. Oshima, Y. Tomioka, and Y. Tokura, Phys. Rev. B **74**, 064419 (2006).

[4.5] H. Aliaga, D. Magnoux, A. Moreo, D. Poilblanc, S. Yunoki, and E. Dagotto, Phys. Rev. B **68**, 104405 (2003).

[4.6] S. Yunoki, T. Hotta, and E. Dagotto, Phys. Rev. Lett. **84**, 3714 (2000).

[4.7] Y. Okimoto, Y. Tomioka, Y. Onose, Y. Otsuka, and Y.Tokura, Phys. Rev. B **57**, R9377 (1998).

[4.8] M. K. Dalai, P. Pal, B. R. Sekhar, N. L. Saini, R. K. Singhal, K. B. Garg, B. Doyle, S. Nannarone, C. Martin, and F. Studer, Phys. Rev. B **74**, 165119 (2006).

[4.9] A. Sekiyama, S. Suga, M. Fujikawa, S. Imada, T. Iwasaki, K. Matsuda, T. Matsushita, K. V. Kaznacheyev, A. Fujimori, H. Kuwahara, and Y. Tokura, Phys. Rev. B **59**, 15528 (1999).

[4.10] A. Biswas, A. K. Raychaudhuri, R. Mahendiran, A. Guha, R. Mahesh, and C. N. R. Rao, J. Phys.: Condens. Mat. **9**, L355 (1997).

[4.11] Y. Tomioka, A. Asamitsu, H. Kuwahara, Y. Moritomo, and Y. Tokura, Phys. Rev. B **53**, R1689 (1996).

[4.12] M. v. Zimmermann, C. S. Nelson, J. P. Hill, D. Gibbs, M. Blume, D. Casa, B. Keimer, Y. Murakami, C.-C. Kao, C. Venkataraman, T. Gog, Y. Tomioka, and Y. Tokura, Phys. Rev. B **64**, 195133 (2001).

[4.13] Z. Jirak, S. Krupica, Z. Simsa, M. Dlouha, and S. Vratislav, J. Magn. Magn. Mater **53**, 153 (1985).

[4.14] A. Asamitsu, Y. Tomioka, H. Kuwahara, and Y. Tokura, Nature **388**, 50 (1997).

[4.15] Y. Moritomo, H. Kuwahara, Y. Tomioka, and Y. Tokura, Phys. Rev. B **55**, 7549 (1997).

[4.16] K. Miyano, T. Tanaka, Y. Tomioka, and Y. Tokura, Phys. Rev. Lett. **78**, 4257 (1997).

[4.17] M. Fiebig, K. Miyano, Y. Tomioka, and Y. Tokura, Science **280**, 1925 (1998).

[4.18] Since for $x = 0.25$ the spectra near E_F was nearly unchanged within the low-temperature FI phase, the charging effect, which causes an energy shift towards higher binding energies, can be excluded. Also, charging effects for $x = 0.3$ and 0.5 were unlikely because the resistivities at 80 K of the $x = 0.3$ and 0.5 samples were lower than that of $x = 0.25$ [Ref. [4.11]; R. Kajimoto, H. Mochizuki, H. Yoshizawa, S. Okamoto, and S. Ishihara, Phys. Rev. B **69**, 054433 (2004)].

[4.19] W. Bao, J. D. Axe, C. H. Chen, and S.-W. Cheong, Phys. Rev. Lett. **78**, 543 (1997).

[4.20] H. L. Liu, S. L. Cooper, and S.-W. Cheong, Phys. Rev. Lett. **81**, 4684 (1998).

[4.21] D. D. Sarma, N. Shanthi, S. R. Krishnakumar, T. Saitoh, T. Mizokawa, A. Sekiyama, K. Kobayashi, A. Fujimori, E. Weschke, R. Meier, G. Kaindl, Y. Takeda, and M. Takano, Phys. Rev. B **53**, 6873 (1996).

[4.22] T. Saitoh, A. Sekiyama, K. Kobayashi, T. Mizokawa, A. Fujimori, D. D. Sarma, Y. Takeda, and M. Takano, Phys. Rev. B **56**, 8836 (1997).

[4.23] G. C. Milward, M. J. Calderon, and P. B. Littlewood, Nature **433**, 607 (2005).